

## THE DESTRUCTION OF COSMOLOGICAL MINIHALOS BY PRIMORDIAL SUPERNOVAE

DANIEL WHALEN<sup>1,4</sup>, BOB VAN VEELEN<sup>2</sup>, BRIAN W. O'SHEA<sup>1,3</sup>, & MICHAEL L. NORMAN<sup>4</sup>

*Draft version November 2, 2018*

### ABSTRACT

We present numerical simulations of primordial supernovae in cosmological minihalos at  $z \sim 20$ . We consider Type II supernovae, hypernovae, and pair instability supernovae (PISN) in halos from  $6.9 \times 10^5 - 1.2 \times 10^7 M_{\odot}$ , those in which Population III stars are expected to form via H<sub>2</sub> cooling. Our simulations are novel in that they are the first to follow the evolution of the blast from a free expansion on spatial scales of  $10^{-4}$  pc until its approach to pressure equilibrium in the relic H II region of the progenitor,  $\sim 1000$  pc. Our models include nine-species primordial chemistry together with all atomic H and He cooling processes, inverse Compton cooling and free-free emission. The supernovae evolve along two evolutionary paths according to whether they explode in H II regions or neutral halos. Those in H II regions first expand adiabatically and then radiate strongly upon collision with baryons ejected from the halo during its photoevaporation by the progenitor. Explosions in neutral halos promptly emit most of their kinetic energy as x-rays, but retain enough momentum to seriously disrupt the halo. We find that the least energetic of the supernovae are capable of destroying halos  $\lesssim 10^7 M_{\odot}$ , while a single PISN can destroy even more massive halos. Blasts in H II regions disperse heavy elements into the IGM, but neutral halos confine the explosion and its metals. Primordial supernova remnants develop dynamical instabilities at early times capable of enriching up to  $10^6 M_{\odot}$  of baryons with metals to levels  $\gtrsim 0.01 Z_{\odot}$ , well above that required for low-mass star formation. In H II regions, a prompt second generation of stars may form in the remnant at radii of 100 - 200 pc in the halo. Explosions confined by large halos instead recollapse, with infall rates in excess of  $10^{-2} M_{\odot} \text{ yr}^{-1}$  that heavily contaminate their interior. This fallback may either fuel massive black hole growth at very high redshifts or create the first globular cluster with a radius of 10 - 20 pc at the center of the halo. Our findings allow the possibility that the first primitive galaxies formed sooner, with greater numbers of stars and distinct chemical abundance patterns, than in current models.

*Subject headings:* cosmology: theory—early universe—hydrodynamics—stars: early type—supernovae: individual

### 1. INTRODUCTION

Numerical studies indicate that primordial stars form in the first pregalactic objects to reach masses of  $\sim 5 \times 10^5 M_{\odot}$  at  $z \sim 20 - 50$  (Bromm et al. 1999; Abel et al. 2000, 2002; Gao et al. 2007). The models suggest that Population III stars form in isolation (one per halo) and that they are likely very massive, from 100 to 500  $M_{\odot}$ . More recent work surveying a larger sample of halos (O'Shea & Norman 2007) extends the lower mass limit of primordial stars down to 15  $M_{\odot}$ . Very massive stars easily photoionize their halos, typically in a few hundred kyr with final H II region radii of 2500 - 5000 pc while H II regions of less massive stars are confined to very small radii ( $< 10^{-3}$  pc) by the high central densities deep in the halo (Whalen et al. 2004; Kitayama et al. 2004; Alvarez et al. 2006; Abel et al. 2007; Johnson et al. 2007; Yoshida et al. 2007; Wise & Abel 2007a,b). In the latter case, high recombination rates and pressure from overlying matter due to the depth of the halo dark matter potential well halts the expansion of the heated

bubble (Franco et al. 1990). Unlike massive stars in the Galaxy today, little mass loss occurs in Population III stars because there are no line-driven winds from their pristine atmospheres (Baraffe, Heger, & Woosley 2001; Kudritzki 2000; Vink, de Koter, & Lamers 2001), although mixing in rapidly rotating stars may cause some mass loss later in their lives (Meynet et al. 2007). Consequently, winds do not clear gas from cosmological halos in the first generation of stars as they do from molecular cloud cores today. However, if the ionization front (I-front) of the star breaks out of the halo it will sweep more than half of the baryons interior to the virial radius into a thick shell  $\sim 100$  pc in radius by the end of the life of the star (Whalen et al. 2004; Kitayama et al. 2004). The diffuse gas enclosed by the shell is uniform and at densities far lower than in the original halo, 0.1 - 1  $\text{cm}^{-3}$  instead of more than  $10^{10} \text{ cm}^{-3}$ .

The ultimate fate of a Population III star depends on its mass at the end of its main sequence lifetime (MSL). Those lying between 10  $M_{\odot}$  and 40  $M_{\odot}$  die in Type II supernova explosions, ejecting roughly 20% of their mass into the intergalactic medium (IGM) as metals and leaving behind a compact remnant. Stars between 140  $M_{\odot}$  and 260  $M_{\odot}$  explode in extremely energetic pair instability supernovae (PISN) hundreds of times more powerful (Heger & Woosley 2002). As much as 50% of the mass of the star is dispersed as heavy elements into the IGM in such events, with no compact remnant. However, these

<sup>1</sup> Applied Physics (X-2), Los Alamos National Laboratory

<sup>2</sup> Astronomical Institute Utrecht, Princetonplein 5, Utrecht, The Netherlands

<sup>3</sup> Theoretical Astrophysics (T-6), Los Alamos National Laboratory

<sup>4</sup> Center for Astrophysics and Space Sciences, University of California at San Diego, La Jolla, CA 92093, U.S.A. Email: dwhalen@lanl.gov

predictions are based on one-dimensional non-rotating stellar evolution models that make a range of assumptions (e. g. mixing parameters) and should be considered qualitative, rather than quantitative, in nature. How far elements are expelled from the star depends strongly on the state of the halo prior to the explosion. Supernova (SN) remnants in halos completely ionized by the star typically expand to half the diameter of the H II region. The shock front comes into pressure equilibrium with the hot recombining gas more quickly than if the blast propagates in a neutral medium of comparable density (Greif et al. 2007).

Supernovae in neutral halos, which result when low-mass Population III stars fail to ionize them, evolve quite differently. Because no winds evacuate gas from the center of the halo, the blast encounters circumstellar densities several orders of magnitude greater than in OB associations in the Galaxy, with much higher energy losses at very early times. Since the blast energy is much greater than the binding energy of the gas in the halo, it is often supposed that PISN easily destroyed halos. Here, destruction of the halo means complete expulsion of its gas, not dispersal of the dark matter itself, which remains mostly undisturbed. However, as Kitayama & Yoshida (2005) point out, this argument ignores radiative losses from the shock in the large densities deep in the halo. They find that bremsstrahlung and inverse Compton cooling (IC) radiate away the explosion’s energy before it even sweeps up its own mass in ambient gas, quenching the blast and preventing any dissemination of metals into the halo. Explosions with hundreds of times the binding energy may be necessary to disperse more massive halos under these conditions.

However, a difficulty with this and other studies of primordial supernovae in cosmological halos is how the explosion itself is initialized. This is typically done by depositing the energy of the blast as thermal energy on the mesh and allowing pressure gradients to launch shocked flows into their surroundings (Bromm et al. 2003; Kitayama & Yoshida 2005; Greif et al. 2007). This is partly justified for explosions in H II regions whose central densities are quite low and in which early radiative losses from the remnant are minimal. Too much energy loss from the early remnant would be ignored by this approach for SN in neutral halos, which cool strongly from very early times due to high ambient densities.

In fact, explosions initialized by thermal pulses in neutral halos cool before any of their energy can be converted into motion (Kitayama & Yoshida 2005). When the energy of the blast is deposited as heat to central mesh zones, their temperatures skyrocket to tens of billions of degrees K, driving extreme bremsstrahlung and IC losses before pressure gradients can accelerate any flows. These initial conditions do not properly represent the free expansion that actually erupts through the stellar envelope and whose momentum cannot be radiated away. The early stages of the explosion in a nearly undisturbed halo are much better modeled by a cold free expansion in which the energy of the blast is kinetic rather than thermal. Furthermore, supernovae modeled in cosmological density fields with smoothed particle hydrodynamics methods (Bromm et al. 2003; Greif et al. 2007) also lack the numerical resolution to capture the early hydrodynamic behavior of the blast wave. Dynamical

instabilities might manifest that lead to early mixing of heavy elements in the ejecta with ambient halo material on much earlier time scales than in current simulations.

How easily neutral halos are destroyed by primordial supernovae and how metals mix with the early IGM thus remains unclear. One key issue is how much gas is displaced in the halo by the momentum of the ejecta after its energy is lost to cooling processes in the expanding flow at early times. In H II regions the shock later strongly interacts with the dense shell of ionized gas expanding within the H II region. How well do metals in the remnant mix with the dense shell, and if dynamical instabilities arise that fragment the shock into enriched clumps, are they liable to collapse into new stars? Numerical simulations excluding these phenomenon indicate that metals do not significantly mix with the IGM until gas falls back into the dark matter potential after about a Hubble time (Greif et al. 2007).

Capturing the true evolution of the blast presents numerical challenges due to the spatial scales at play. To accurately represent the initial ejecta as a free expansion, its hydrodynamical profile cannot extend beyond radii that enclose more surrounding gas than ejecta mass. In the high central densities of neutral halos such radii are  $5 \times 10^{-4} - 1 \times 10^{-3}$  pc, but the blast must then be evolved to tens or hundreds of parsecs to evaluate its true impact on the halo. Furthermore, multiple sites of intense luminosity will erupt in the flow over all these scales from the earliest times, so the chemistry of the flow must be solved consistently with hydrodynamics to determine where gas is collisionally ionized and therefore strongly radiating. The attendant time scales can restrict integration times to much lower values than Courant times.

To address these questions we have performed one-dimensional models of Type II supernovae, hypernovae, and PISN in neutral and ionized cosmological halos at redshift 20. Our initial conditions are spherically-averaged halos derived from cosmological initial conditions with the Enzo adaptive mesh refinement (AMR) code (O’Shea et al. 2004) that are photoionized by the star in the ZEUS-MP reactive flow radiative transfer code (Whalen & Norman 2006). The aim of our survey is to determine the explosion energies required to destroy cosmological halos that are thought to form primordial stars by H<sub>2</sub> cooling. We also evaluate their observational signatures and how their metals will mix with the ambient medium as a prelude to three-dimensional AMR calculations now in progress.

Our radiation hydrodynamics scheme and initial profiles for the free expansion are presented in § 2. We also describe the expanding grids used in this study and the time-dependent boundary conditions that present the ambient medium to the expanding flow. H II region profiles for the explosions and the grid of supernova and halo models selected for this survey are outlined in § 3. The evolution of blasts in both neutral halos and H II regions are examined together with dominant energy loss mechanisms for each case in § 4. We discuss observational measures for both kinds of explosion in § 5, chemical enrichment of baryons in the halos in § 6 and conclude in § 7.

## 2. NUMERICAL METHOD

Three-dimensional halo baryon profiles computed from cosmological initial conditions are extracted from an Enzo AMR run and spherically averaged into one-dimensional density fields. These profiles are then photoionized over the main sequence lifetime of the SN progenitor with the ZEUS-MP astrophysical fluid hydrodynamics code. We then initialize one-dimensional explosion profiles in the ionized halos and evolve the blasts in a separate calculation. ZEUS-MP has been modified to solve explicit finite-difference approximations to Euler's equations of fluid dynamics coupled to 9-species primordial chemistry with photoionization rate coefficients computed from multifrequency photon-conserving UV transport (Whalen & Norman 2007b). The fluid equations are

$$\frac{\partial \rho}{\partial t} = -\nabla \cdot (\rho \mathbf{v}) \quad (1)$$

$$\frac{\partial \rho v_i}{\partial t} = -\nabla \cdot (\rho v_i \mathbf{v}) - \nabla p - \rho \nabla \Phi - \nabla \cdot \mathbf{Q} \quad (2)$$

$$\frac{\partial e}{\partial t} = -\nabla \cdot (e \mathbf{v}) - p \nabla \cdot \mathbf{v} - \mathbf{Q} : \nabla \mathbf{v} \quad (3)$$

where  $\rho$ ,  $e$ , and the  $v_i$  are the mass density, internal energy density, and velocity components of each zone, and  $p = (\gamma-1)e$  and  $\mathbf{Q}$  are the gas pressure and the von Neumann-Richtmeyer artificial viscosity tensor (Stone & Norman 1992).

Nine additional continuity equations are solved to advect H, H<sup>+</sup>, He, He<sup>+</sup>, He<sup>++</sup>, H<sup>-</sup>, H<sub>2</sub><sup>+</sup>, H<sub>2</sub>, and e<sup>-</sup>, which are assumed to share a common velocity distribution. Thirty reactions among these primordial species are followed with the nonequilibrium rate equations of Anninos et al. (1997)

$$\frac{\partial \rho_i}{\partial t} = \sum_j \sum_k \beta_{jk}(T) \rho_j \rho_k + \sum_j \kappa_j \rho_j \quad (4)$$

where  $\beta_{jk}$  is the rate coefficient of the reaction between species  $j$  and  $k$  that creates (+) or removes (-) species  $i$ , and the  $\kappa_j$  are the ionization rates. The continuity equations for each reactant are updated in the advection routines and the reaction network is evolved in a separate operator-split semi-implicit substep. We enforce charge and baryon conservation at the end of each hydrodynamic cycle by assigning any error between the species or charge sums and  $\rho$  to the largest of the species to bring them into agreement with  $\rho$ . Microphysical cooling and heating are included with an isochoric operator-split update to the energy density evaluated each time the reaction network is solved:

$$\dot{e}_{\text{gas}} = \Gamma - \Lambda \quad (5)$$

Here,  $\Gamma$  is the rate at which photons at all frequencies in the calculation deposit heat into the gas as described in Whalen & Norman (2007b) and  $\Lambda$  is the sum of the cooling rates due to collisional ionization and excitation of H and He, recombinations in H and He, inverse Compton scattering (IC) from the CMB, and bremsstrahlung emission. H<sub>2</sub> cooling (Galli & Palla 1998) is included in the H II region calculation but not in the evolution of the

SN blast, whose high temperatures and strong shocks destroy the fragile hydrogen molecules on the time scales of our models. We do not include metal line cooling, but reserve it for three-dimensional models now in preparation.

Photon-conserving UV transport in the spherical polar coordinate grid used in this study is performed by solving the static approximation to the equation of radiative transfer in flux form

$$\nabla \cdot \mathbf{F} = -\chi \mathbf{F}_r, \quad (6)$$

where  $\chi$  is the inverse mean free path of a UV photon in the neutral gas

$$\chi = \frac{1}{n\sigma}, \quad (7)$$

to compute the total absorption rate in each zone by photon conservation, which mandates that the number of absorptions in a zone is equal to the photons entering the zone minus those exiting each second. In terms of flux, this difference reduces to

$$n_{\text{abs}} = F_i \left( 1 - e^{-\chi(r_{i+1}-r_i)} \right) \times \frac{r_i^2 (\phi_{k+1} - \phi_k) (\cos \theta_j - \cos \theta_{j+1})}{h\nu} \quad (8)$$

Individual interaction rates (photoionizations, photodetachments, and photodissociations) are obtained from the total rate according to the prescription

$$n_i = \frac{1 - e^{-\tau_i}}{\sum_{i=1}^n 1 - e^{-\tau_i}} n_{\text{abs}}. \quad (9)$$

which are then converted into the photoionization rate coefficients required by the reaction network

$$k_i = n_i \cdot \frac{1}{n_{\text{spec}} V_{\text{cell}}}, \quad (10)$$

where  $n_{\text{spec}}$  is the number density of the species with which the photons are interacting. We adopt the on-the-spot (OTS) approximation by assuming that recombinations to the ground state balance photoionizations by diffuse photons within a zone, so we do not explicitly transport recombination radiation. Complete descriptions of the photon conserving UV transport from which radiative rates in the reaction network are derived can be found in Whalen & Norman (2006, 2007b).

### 2.1. Free-Expansion Blast Profiles

We take density and velocity profiles for the free expansion from Truelove & McKee (1999), where it is shown that at a given time the ejecta density can be approximated by a flat inner core and steeply declining outer edge:

$$\rho(v, t) = \begin{cases} F \cdot t^{-3} & \text{for } v \leq v_{\text{core}} \\ F \cdot t^{-3} \cdot \left(\frac{v}{v_{\text{core}}}\right)^{-n} & \text{for } v_{\text{core}} < v \leq v_{\text{max}} \\ 0 & \text{for } v > v_{\text{max}} \end{cases}, \quad (11)$$

$$v(r, t) = \frac{r}{t} \text{ for } t > 0. \quad (12)$$

Here,  $\rho$  is the density,  $t$  is the time,  $v$  is the velocity and  $r$  is the radius.  $F$  and  $v_{\text{core}}$  are normalization constants which must be determined. The time dependence in the density is due to the expansion of the ejecta: as it grows in volume by  $r^3$  its density decreases by  $r^{-3} \propto t^{-3}$ . The inner region of the free expansion,  $v \leq v_{\text{core}}$ , has a constant density and the outer region,  $v > v_{\text{core}}$ , decreases by a power law with index  $n$ . Such profiles, with  $n = 9$ , are usually assumed for core collapse supernovae (Truelove & McKee 1999; Dwarkadas 2005; Chugai & Chevalier 2006). The early evolution of the blast is insensitive to the choice of  $r_{\text{max}}$ , unless it exceeds the radius enclosing an ambient mass greater than the ejecta mass.

The two normalization constants,  $F$  and  $v_{\text{core}}$ , are determined from the ejecta mass  $M_{\text{ej}}$  and energy  $E_{\text{ej}}$ . The energy is assumed to be entirely kinetic. To calculate these constants we first choose a maximum radius  $r_{\text{max}}$  ( $> 0$ ) that defines the leading edge of the SN ejecta and a maximum velocity  $v_{\text{max}}$  for the remnant. This radius is a free parameter and is usually set so that the enclosed baryonic mass in the halo equals  $M_{\text{ej}}$ . The maximum velocity is set to  $3 \times 10^4$  km/s, corresponding roughly to that observed in core-collapse supernova explosions. We set  $r_{\text{min}} = 0$  in all our models.

To determine  $F$  and  $v_{\text{core}}$ , we first set  $t = t_{\text{max}} = r_{\text{max}}/v_{\text{max}}$ , the time by which the leading edge of free expansion has self-similarly grown to  $r_{\text{max}}$ , the initial radius we have chosen for the blast. Using equations 11 and 12 and choosing  $F = 1$  and  $v_{\text{core}}$  to be some small arbitrary value, we perform the following integrations:

$$M_{\text{ej}} = \int_{r_{\text{min}}}^{r_{\text{max}}} 4\pi r^2 \cdot \rho(v, t) dr. \quad (13)$$

$$E_{\text{ej}} = \int_{r_{\text{min}}}^{r_{\text{max}}} 4\pi r^2 \cdot \frac{1}{2} \rho(v, t) v(t)^2 dr, \quad (14)$$

Neither of these integrations will return correct values for  $M_{\text{ej}}$  and  $E_{\text{ej}}$  at first because  $F$  and  $v_{\text{core}}$  were arbitrarily chosen. Selecting a new  $F'$  equal to  $M_{\text{ej}}$  divided by the mass obtained from Eq. 13, which guarantees the first integration equals the correct ejecta mass by construction, we repeat the second integration and check if it is equal to  $E_{\text{ej}}$ . If so,  $F'$  and  $v_{\text{core}}$  are those needed to construct the density profile. If not, we increase the value for  $v_{\text{core}}$ , again set  $F = 1$ , obtain a new  $F'$ , which partly depends on the new  $v_{\text{core}}$ , from the first integral, and then compute a new  $E_{\text{ej}}$  with the second integral. We repeat this two-step procedure until the latest choice of  $v_{\text{core}}$  and  $F'$  returns the correct value of  $E_{\text{ej}}$  in the second integration; the  $F'$  in this final cycle is the  $F$  we apply to the density profile on the grid. Once we have  $F$  and  $v_{\text{core}}$ , and recalling that  $t = t_{\text{max}} = r_{\text{max}}/v_{\text{max}}$  and  $v = r/t_{\text{max}}$ , we recast eq 11 as a function of  $r$  in order to initialize densities on the grid.

Analytical expressions can be found for the normalization constants  $F$  and  $v_{\text{core}}$  without resorting to iteration in certain circumstances. Equations (11) and (12) can be substituted into Equations (14) and (13) to obtain

$$M_{\text{ej}} = 4\pi t_{\text{max}}^{-3} F \left( \frac{r_{\text{core}}^3 - r_{\text{min}}^3}{3} - r_{\text{core}}^n \frac{(r_{\text{max}}^{3-n} - r_{\text{core}}^{3-n})}{3-n} \right), \quad (15)$$

$$E_{\text{ej}} = 2\pi t_{\text{max}}^{-5} F \left( \frac{r_{\text{core}}^5 - r_{\text{min}}^5}{5} - r_{\text{core}}^n \frac{(r_{\text{max}}^{5-n} - r_{\text{core}}^{5-n})}{5-n} \right), \quad (16)$$

Here,  $t_{\text{max}} = r_{\text{max}}/v_{\text{max}}$ ,  $r_{\text{core}} = v_{\text{core}} \cdot t_{\text{max}}$  and  $r_{\text{min}}$  and  $r_{\text{max}}$  are the minimum and maximum radius of the free expansion, respectively. If  $r_{\text{min}} \ll r_{\text{core}} \ll r_{\text{max}}$ , which is generally true, then  $F$  and  $v_{\text{core}}$  can be expressed as (Truelove & McKee 1999):

$$v_{\text{core}} = \frac{r_0}{t_{\text{core}}} = \left( \frac{10E_{\text{ej}}(n-5)}{3M_{\text{ej}}(n-3)} \right)^{\frac{1}{2}}, \quad (17)$$

$$F = \frac{1}{4\pi n} \cdot \frac{(3(n-3)M_{\text{ej}})^{\frac{5}{2}}}{(10(n-5)E_{\text{ej}})^{\frac{3}{2}}} = \frac{10(n-5)E_{\text{ej}}}{4\pi n} \cdot v_{\text{core}}^{-5}. \quad (18)$$

We iterate to find  $F$  and  $v_{\text{core}}$  because the assumptions underlying the analytical forms might not be satisfied for all ejecta profiles discretized on a mesh. At times  $r_{\text{core}}$  could lie close to the inner or outer boundary of the grid. In this case the analytical solution is different from the one found iteratively and could introduce errors in the mass and energy on the grid if applied. To prevent such errors we always solve for  $F$  and  $v_{\text{core}}$  numerically.

## 2.2. Moving Grid/Boundary Conditions

As noted earlier, to realistically represent the early remnant as a free expansion in neutral halos it cannot enclose more halo gas than its own mass in ejecta, which confines its initial extent to less than 0.001 pc if the halo. This restriction is problematic, given that its expansion must be accurately resolved out to the virial radius of the halo,  $\sim 100$  pc. However, this can be accomplished with a fixed number of mesh points if the grid itself expands with the flow and always maintains its outer boundary beyond the expanding shock front. In this scenario only the surrounding halo just beyond the shock can be present on the grid at any time, so as the outer boundary of the grid grows with time its densities, energy, and velocities must be updated according to its given position within the halo. In this way the expanding flow always encounters the densities it would if the entire halo resided on the grid. An additional benefit is that Courant times become longer as the grid grows, accelerating the execution of the calculation.

We activate moving grids in the radial coordinate in ZEUS-MP for the models in this study, modifying the outer boundary conditions every hydrodynamical time step with an operator-split update following the calculation of a new grid. At the start of the simulation we allocate 80% of the mesh to the free expansion profile, reserving the outer 20% for the ambient halo. Every time step thereafter the outer 10% of the grid is swept for the maximum radial gas velocity and its position on the mesh. A grid velocity describing homologous expansion is then assigned to each grid point such that the grid

TABLE 1  
HALOS

halo	$J_{\text{LW}}$	$M (M_{\odot})$	$z_{\text{coll}}$	$E_{\text{B}}$ (erg)
1	0	6.9E+05	24.1	1.53E+49
2	3.16E-23	2.1E+06	20.4	1.10E+50
3	1.00E-21	1.2E+07	17.3	2.50E+51

velocity at the radius of the previous maximum in gas velocity is three times this maximum. The factor of 3 guarantees that the flow never reaches the outer boundary, where inflow conditions are reset each time step to ensure the remnant always encounters the correct ambient medium. If the velocity of the grid is non-zero, the entire radial grid is updated in the following manner. First a new outer boundary is determined from the old boundary, the grid velocity and the current time step. A new grid is then computed such that the radial cells, whose number remains fixed, are redistributed equally over the new range in radius. See Hayes et al. (2006) for a discussion of ZEUS-MP’s moving Eulerian grid option.

Species densities, energies, and velocities on the outer boundary are updated each hydrodynamical time step by interpolating from a data table whose entries are binned by radius. The profiles in these tables are those of the halo photoionized by the original star over its main sequence lifetime, which were computed in the separate calculation with nine-species primordial chemistry and radiative transfer that was described above. The flow values assigned to the outer boundary depend upon the position bin into which the boundary falls at a given time step. We describe the stellar masses and halos used in our models in the following section.

### 2.3. Static Dark Matter Potential

Primordial supernova remnants evolved in much deeper gravitational potentials due to dark matter than SN in the galaxy today. Gravitational potentials in the halos in our study are dominated by baryons at radii of less than a parsec and by dark matter at larger radii. We neglect the self-gravity of the remnant on scales below a parsec because of its large kinetic energy but include the potential of the dark matter on all scales. Since merger times at  $z \sim 20$  are approximately 20 Myr, much longer than the dynamical times of the remnant, to good approximation the gravitational potential of the dark matter can be held fixed in our simulations. We interpolate the dark matter potential of the halo onto the initial grid at the beginning of the run and onto each new grid thereafter, but the potential itself never evolves. We apply this potential to force updates to the gas velocities throughout the calculation. The interpolation substep is operator split from the time-dependent boundary updates of the fluid variables described above.

## 3. SN PROGENITOR H II REGIONS

The halos adopted for our study were taken from O’Shea & Norman (2007), who examined the formation of Pop III stars in a range of Lyman-Werner (LW) backgrounds (11.18 - 13.6 eV). Since more baryons are required to shield  $\text{H}_2$ -cooled cores from dissociation as the LW background rises, the minimum halo mass required to form a star rises with decreasing redshift. We consider

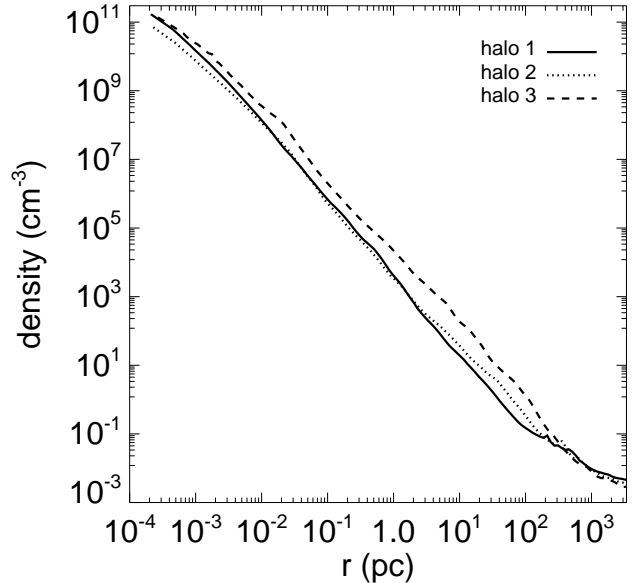


FIG. 1.— Spherically-averaged baryon density profiles for the halos examined in this study.

TABLE 2  
SN PROGENITORS

$M (M_{\odot})$	$t_{\text{MSL}}$ (Myr)	$\log T_{\text{eff}}$	$\log L/L_{\odot}$	$\dot{n}_{\text{ph}}$ ( $\text{s}^{-1}$ )
15	10.4	4.759	4.324	1.861E+48
40	3.864	4.900	5.420	2.469E+49
260	2.106	5.004	6.721	3.272E+50

three different halos that span the masses for which Pop III stars are expected to form by  $\text{H}_2$  cooling. Their properties are summarized in Table 1 and their spherically-averaged baryon density profiles are shown in Figure 1. In column 1, we list the halo number, in column 2 the LW background in which they form, in column 3 their mass, in column 4 their redshift, and in column 5 their binding energy. SN progenitors were chosen according to the types of explosions that were possible in primordial halos:  $15 M_{\odot}$  (Type II supernova),  $40 M_{\odot}$  (hypernovae), and  $260 M_{\odot}$  (PISN). Their properties are tabulated in Table 2 (Schaerer 2002). To obtain accurate circumstellar media for the supernovae, each star was allowed to ionize each halo and then explode, for a total of nine models listed in Table 3. In Table 1  $J_{\text{LW}}$  is the mean intensity of LW photons in which the halos form, centered at 12.87 eV in units of  $\text{erg}^{-1} \text{cm}^{-2} \text{Hz}^{-1} \text{sr}^{-1}$  and  $z_{\text{coll}}$  is the redshift at which the star appears in the halo. The binding energy of the gas  $E_{\text{B}}$  in each halo can be approximated by that of a homogeneous sphere, which is given by

$$E_{\text{B}} = \frac{3}{5} \frac{GM_{\text{h}}m_{\text{b}}}{R_{\text{vir}}}, \quad (19)$$

where  $M_{\text{h}}$  and  $m_{\text{b}}$  are the total halo and baryon masses, respectively, and  $R_{\text{vir}}$  is the virial radius of the halo. In Table 2  $\dot{n}_{\text{ph}}$  is the total number of ionizing photons emitted per second.

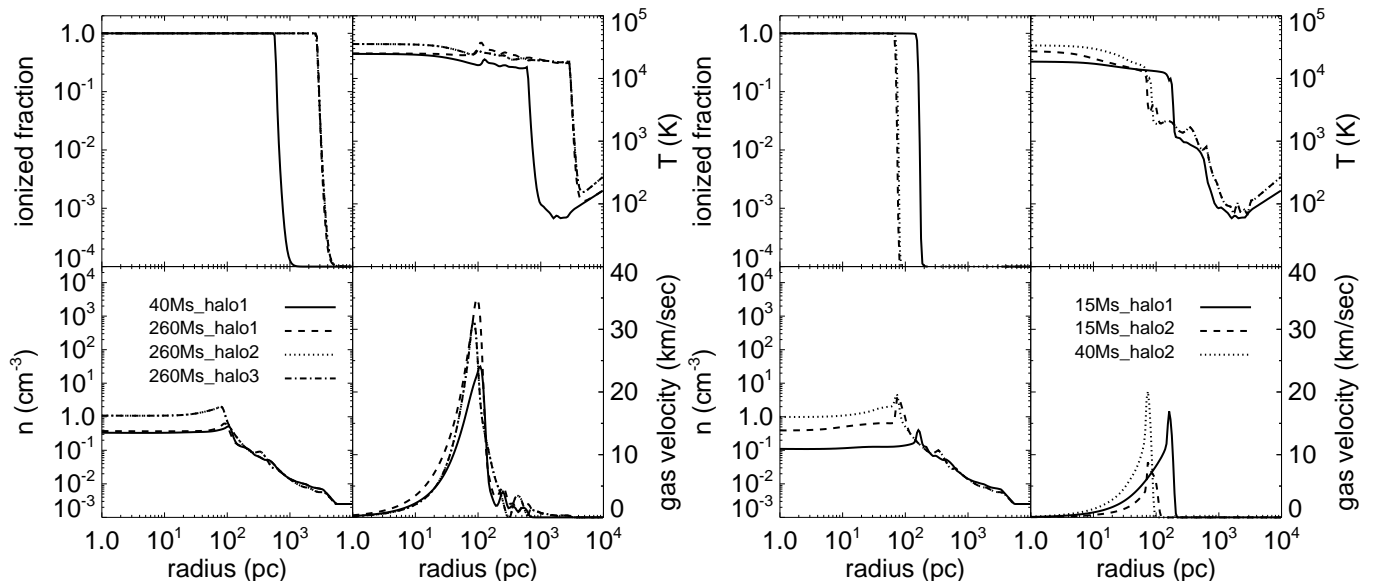


FIG. 2.— Density, temperature, ionization fraction, and velocity profiles of the SN progenitor H II regions at the end of the life of the stars. Left: H II regions that break out of the halo. Solid: 40Ms\_halo1; dashed: 260Ms\_halo1; dotted: 260Ms\_halo2; dot dash: 260Ms\_halo3. Right: H II regions that are confined to the virial radius of the halo. Solid: 15Ms\_halo1; dashed: 15Ms\_halo2; dotted: 40Ms\_halo2. Since the H II region radii of the 15  $M_{\odot}$  and 40  $M_{\odot}$  stars in halo 3 are below the resolution limit of the radiation calculation, their hydrodynamical profiles are considered to be those of the neutral halo.

TABLE 3  
PRIMORDIAL SN EXPLOSION MODELS

halo	15 $M_{\odot}$	40 $M_{\odot}$	260 $M_{\odot}$
1	15Ms_halo1	40Ms_halo1	260Ms_halo1
2	15Ms_halo2	40Ms_halo2	260Ms_halo2
3	15Ms_halo3	40Ms_halo3	260Ms_halo3

### 3.1. Problem Setup

The star was centered in a 200 zone one-dimensional spherical coordinate mesh with reflecting and outflow inner and outer boundary conditions, respectively. Cell sizes were ratioed by the parameter  $\beta$  according to the prescription

$$\frac{\Delta r_{i+1}}{\Delta r_i} = \beta. \quad (20)$$

We applied  $\beta$  from 1.049 to 1.055 to concentrate zones at the origin, both to resolve the central core and density drop and to obtain the maximum time step capable of accurately capturing the emergence of the I-front from the core. The outer boundary in all the H II region models was 10 kpc and the inner boundary of each model was chosen to enclose a volume at the center of the neutral halo equal in mass to the star. In doing so, we assume that all of this enclosed gas goes into forming the star and that the densities just beyond this volume are those that the nascent I-front encounters. In lieu of more accurate models of the environment of the newborn star, these measures ensure the I-front breaks out into the proper ambient densities. For a given star and halo, the inner boundary for the H II region calculation is thus different for the inner boundary chosen for the explosion, which is zero in our models as noted in section 2.1. This choice

is inappropriate for the H II region calculation because it would present higher initial densities to the emerging front than it really encounters. The inner problem radii vary from  $2.6 \times 10^{-3}$  -  $1.4 \times 10^{-2}$  pc.

Forty equally-spaced energy bins were allocated to the radiation transport from 0.755 eV to 13.6 eV and 80 logarithmically-spaced bins were partitioned from 13.6 eV to 90 eV. We found it necessary to include all nine species in our UV breakout models. Breakout of the I-front from the 15  $M_{\odot}$  star is borderline in the more massive halos and may be prevented if a dense shell forms in the front by H<sub>2</sub> cooling. However, H<sub>2</sub> chemistry is problematic at the inner boundary as photons propagate through the central zone. The hard UV spectrum significantly broadens the emergent front, resulting in a protracted period of partial ionization at warm temperatures in the first zone. This, together with very large central densities, results in unrealistically high H<sub>2</sub> formation rates that violate species conservation. This difficulty was eliminated by simply turning off H<sub>2</sub> chemistry until the central zone was completely ionized. Each model was evolved for the main sequence lifetime of the star in the halo. We tabulate final H II region radii for each model in Table 4. Final densities, temperatures, ionization fractions, and velocities for all runs in which H II regions form are shown in Figure 2.

### 3.2. H II Region Breakout

The H II regions in this survey fall into two classes. Those confined to the virial radius of the halo or less and are bounded by subsonic D-type fronts are shown in the right panel of Figure 2. Those that flash-ionize the halo on relatively short time scales and propagate into the IGM as supersonic R-type fronts appear in the left panel of Fig 2. The I-fronts of very massive primordial

TABLE 4  
H II REGION RADII (PC)

halo	15 $M_{\odot}$	40 $M_{\odot}$	260 $M_{\odot}$
1	161.5	599.2	2843
2	70.1	74.1	2694
3	—	—	2694

stars in cosmological halos first transform from R-type to D-type at radii of less than a parsec but then revert back to R-type in a few hundred kyr and completely overrun the halo (Whalen et al. 2004; Kitayama et al. 2004). The I-front exits so rapidly that steep drops in the halo density profile are frozen in place as they are ionized. Once ionized and isothermal, the density gradients become large pressure gradients that launch shocked flows outward from the center. Ionized core shocks can evict more than half of the baryons from the virial radius of the halo over the lifetime of the star, piling the gas up into a dense shell that surrounds an evacuated cavity of very diffuse gas ( $\lesssim 0.1 \text{ cm}^{-3}$ ). This is evident for the 260  $M_{\odot}$  star in halos 1, 2 and 3 in the left panel of Figure 2, which are ionized out to kpc scales. The velocity of the ionized core shock is determined both by the postfront temperature and the slope of the density profile when ionized: it is typically 20 - 40  $\text{km s}^{-1}$ . We note that the 40Ms\_halo1 model is an intermediate case in that the R-type front breaks through the neutral shell just at the end of the star’s life and barely overruns the halo.

### 3.3. Trapped H II Regions

Less massive stars drive weaker I-fronts that either do not revert to R-type or even propagate into the halo at all, as in the case of the 15  $M_{\odot}$  or 40  $M_{\odot}$  stars in halo 3. At the inner radii at which we initialize the respective H II region calculations (2.0e-3 - 0.01 pc), the densities in halo 3 are 2 - 5 times greater than those in halo 1, so recombination rates are greater there by a factor of 4 - 25. There is also more pressure downward on the H II region bubble in halo 3 because there is more overlying matter in its deeper potential well. The lower photon emission rates of the 15  $M_{\odot}$  and 40  $M_{\odot}$  stars cannot compete with these effects, and the H II region radius remains below the resolution limit of the radiation calculation. Not even an ultracompact (UC) H II region forms, so we take the halo to be essentially neutral and undisturbed at the end of the life of the star. In contrast, the I-fronts in the 15Ms\_halo1, 15Ms\_halo2, and 40Ms\_halo2 models do escape the core but cannot escape the virial radius. They remain D-type, as seen in the relative positions of the breaks in the ionization fractions and the shocks in the right panel of Figure 2. The density structure of the D-type fronts differs from the R-type fronts above. Since the expansion rate of the dense neutral is subsonic with respect to the sound speed in the H II region, acoustic waves level the densities in the ionized gas to flat uniform values as the shock expands.

We expect a supernova remnant’s greatest energy losses in H II regions to occur upon impact with the shocked neutral or ionized shell. Prior to its encounter with the shock the remnant will generally experience greater radiative cooling in H II regions bounded by D-type fronts than in halos that are flash-ionized because

their interiors have somewhat higher densities. However, to first order the effect of any H II region that forms in a cosmological halo is to greatly reduce the ambient densities into which the SN ejecta erupt, from  $\sim 10^{11} \text{ cm}^{-3}$  to  $\lesssim 1 \text{ cm}^{-3}$ . This prolongs the free-expansion of the blast and delays cooling. Radiative and losses in neutral halos will be prompt because the remnant initially encounters much higher densities than in H II regions. In the majority of our models, the H II region of the star drives most of the baryons from the halo by photoevaporation, but a supernova explosion is still necessary to remove 90% of the gas from the halo, which is the criterion for its destruction (Kitayama & Yoshida 2005). The final density, energy, velocity, and abundance profiles for each H II region are tabulated in data files. The time-dependent outer boundary updates interpolate these data to ensure that the SN remnant expands into the correct ambient medium.

## 4. SN BLAST WAVE EVOLUTION

The Truelove & McKee (1999) free-expansion solution for the supernova blast is completely parametrized by the mass, kinetic energy, and maximum velocity of the ejecta, which are listed in Table 5 (Heger & Woosley 2002; Tominaga et al. 2007). We also include the mass of the heavy elements expelled by each supernova,  $M_{\text{el}}$ , in Table 5. It should be noted that pair-instability blast energies are not well constrained in present stellar evolution models, and that while the star is thought to be completely dispersed it is not clear how much of its mass goes into the ejecta. For simplicity, we assume that all the mass of the PISN progenitor is in the free expansion. We overlay initial density and velocity profiles for the 15Ms\_halo3 and 40Ms\_halo1 models in Figure 3. Note the enormous disparity in ambient density between blasts initialized in neutral halos and in H II regions. We adopt a power law  $n = 9$  in eq 11 for all of our blast profiles. The free expansion is initialized on a spherical coordinate mesh with 250 uniform zones with reflecting and outflow boundary conditions, respectively. The free expansion occupies the first 200 zones and is joined directly without smoothing or interpolation to the circumstellar medium, which occupies the outer 50 zones. The temperature of the ejecta is set to 1000 K (the temperature of the ambient medium is determined by the gas energy density interpolated in each zone from the halo table data). Since it is relatively cool, the ejecta is assumed to be nearly neutral, with only the small ionization fraction  $\sim 10^{-4}$  expected for primordial gas at  $z \sim 20$ . In reality, whether the ejecta is ionized or neutral matters little because the energy required for its complete ionization is only a small fraction of the energy of the blast and is not significant to its kinematics, as will be shown later.

We deactivate the transport of ionizing radiation during the evolution of the ejecta but retain nine-species primordial chemistry and gas energy updates due to radiative cooling with the hydrodynamics. Collisional excitation and ionization cooling of H, He, and  $\text{He}^+$ , recombination cooling of  $\text{H}^+$ ,  $\text{He}^+$ , and  $\text{He}^{++}$ , bremsstrahlung cooling, and inverse Compton cooling are included in the energy equation. The inner boundary of each problem was  $r = 0$  and the outer boundary was that which would enclose a volume of neutral halo equal in mass to the ejecta, whether or not the halo is ionized by the star.

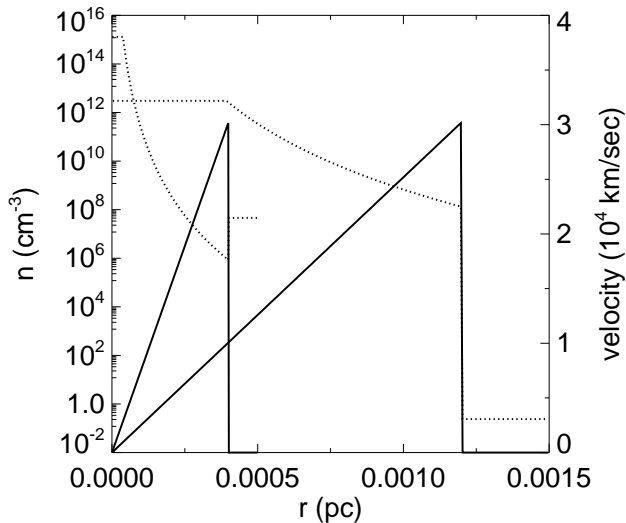


FIG. 3.— Density and velocity profiles of two free expansion blast profiles used in this study. Left: 15Ms\_halo3; right: 40Ms\_halo1. Dotted: number density; solid: velocity.

TABLE 5  
BLAST PARAMETERS

star	$M_{\text{ej}} (M_{\odot})$	$M_{\text{el}} (M_{\odot})$	$E_{\text{ej}} (M_{\odot})$	$v_{\text{max}} (\text{km s}^{-1})$
15 $M_{\odot}$	13.52	5.94	1.0E+51	30000
40 $M_{\odot}$	34.43	20.43	3.0E+52	30000
260 $M_{\odot}$	260	125.27	1.0E+53	30000

For halos 1 and 3 the outer problem radius was 0.0005 pc and for halo 2 it was 0.0015 pc, whether or not the halo was ionized by the progenitor. This guarantees that the blast has not yet swept up its own mass in the halo or departed from a free expansion, and that all energy losses from the remnant are captured from the earliest times. Such small radii for the outer boundary are unnecessary for explosions in H II regions, in which blasts remain free expansions for a parsec or more, but are adopted anyway for simplicity.

Primordial supernovae in cosmological halos follow two distinct evolutionary paths depending on whether they explode in neutral clouds or in H II regions. We now examine the evolution of each type of remnant.

#### 4.1. Supernovae in H II Regions

In Figures 4 and 5 we show four stages of a 260  $M_{\odot}$  pair-instability supernova in halo 1, which is completely ionized by the progenitor. We show in Figure 6 cumulative radiation losses together with kinetic energy for all nine models. The radiative processes tallied are H, He, and He<sup>+</sup> collisional excitation and ionization losses, bremsstrahlung, and IC scattering from the CMB.

##### 4.1.1. $t < 10$ yr: Initial Shock

Even though its surroundings are diffuse,  $n \lesssim 0.1 \text{ cm}^{-3}$ , the free expansion drives a shock into the H II region that

heats immediately to over  $10^{11}$  K, as shown in Figure 4c. The shocked gas is collisionally ionized and accelerates to  $67000 \text{ km s}^{-1}$ . This occurs because the abrupt drop in density at  $r \sim 0.004$  pc in the initial blast profile generates a sharp pressure gradient when it is ionized, and hence isothermal. The gradient accelerates the small amount of gas lying within it to nearly three times its original velocity, driving a rarefaction wave backward into the denser gas behind that is visible in the velocity profile at  $r \sim 0.0045$  pc at  $t = 2.9$  days. The drop in velocity of the dense gas in this wave and the speedup at the edge of the expansion are insignificant compared to the blast energy, so the kinetic energy of the ejecta remains steady for  $t < 700$  yr, as seen in the solid black plot in Figure 6g. The temperature of the ionized gas in the rarefaction wave falls from  $10^{11} - 2 \times 10^9$  K at 2.9 days and then to  $7 \times 10^8$  K by 14.5 days in exchange for  $PdV$  work on its surroundings. We note that the density jump conditions for a strong shock are satisfied at  $r \sim 0.0075$  pc at 14.5 days.

The early H and He excitational losses over  $t < 10$  yr in Figure 6g are due to the ionization of forward edge of the ejecta. They are minute compared to the kinetic energy of the ejecta, which freely expands until it has swept up its own mass in the H II region at a radius of  $\sim 20$  pc. The 'broken sawtooth' velocity profile at 2.9 and 14.5 days soon relaxes into a new free expansion with a peak velocity of  $55000 \text{ km s}^{-1}$ .

##### 4.1.2. 500 yr $< t < 6350$ yr: End of the Free Expansion

At 515.6 yr a homologous free expansion can still be seen in the density profile, which retains a flat central core and power-law dropoff. At this point its radius is only 7.5 pc and the blast has not yet accumulated its own mass in the relic H II region. By 3093 yr it grows to 21 pc and has swept up 260  $M_{\odot}$ . This marks the end of the free expansion: the density profile flattens out and a reverse shock forms at  $r = 16$  pc. The reverse shock strengthens, backstepping through and completely ionizing the remnant as shown in Figures 4f and 4h. As this reverse shock propagates backward through the ejecta from 500 - 6000 yr in Figure 4e, collisional ionization losses in H and He rise over approximately the same interval of time in Figure 6g. We note that at 6347 yr the density profile is reminiscent of the Chevalier phase in galactic SN remnants: a forward shock and reverse shock separated by a contact discontinuity (Chevalier 1974). Inverse Compton scattering with the cosmic microwave background (CMB) begins to remove energy from the hot, ionized interior of the blast after 1 kyr as it grows in volume. Compton losses reach 20% of the energy of the explosion in this run, raising the possibility of small scale fluctuations in the CMB that might be observable through the Sunyaev-Zel'dovich (SZ) effect. We examine this issue in greater detail in § 5.

In this era, the remnant is still well short of the dense shell, and has thus evolved in a uniform medium, as shown in the left panel of Figure 2, which shows the density profile of the H II region. Although not included in Figures 4 and 5 for brevity, reflected shocks traverse the interior of the remnant twice before it reaches the shell. They are less important to the dynamics of the remnant than the adiabatic expansion against the surrounding material, but as will be shown later, they never

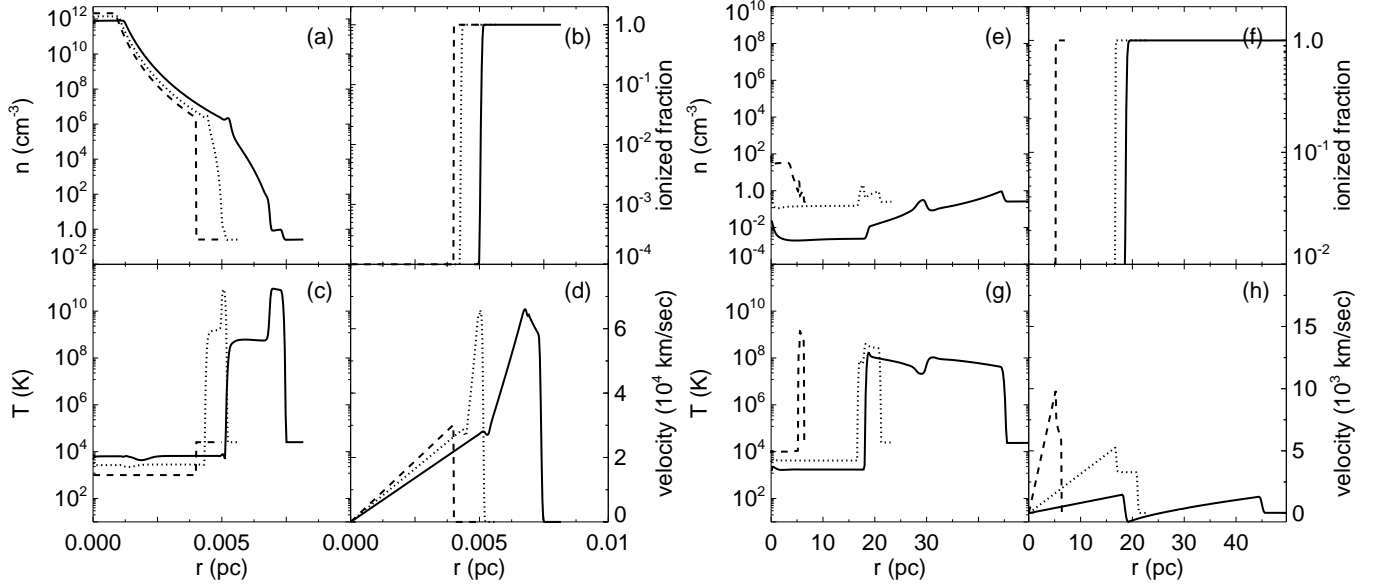


FIG. 4.— Early evolution of the  $260 M_{\odot}$  pair-instability supernova in halo 1. Panels (a) - (d): early free expansion. Dashed:  $t = 0$ ; dotted: 2.9 days; solid: 14.5 days. Panels (e) - (h): end of the free expansion. Dashed:  $t = 515.6$  yr; dotted:  $t = 3093$  yr; solid:  $t = 6347$  yr.

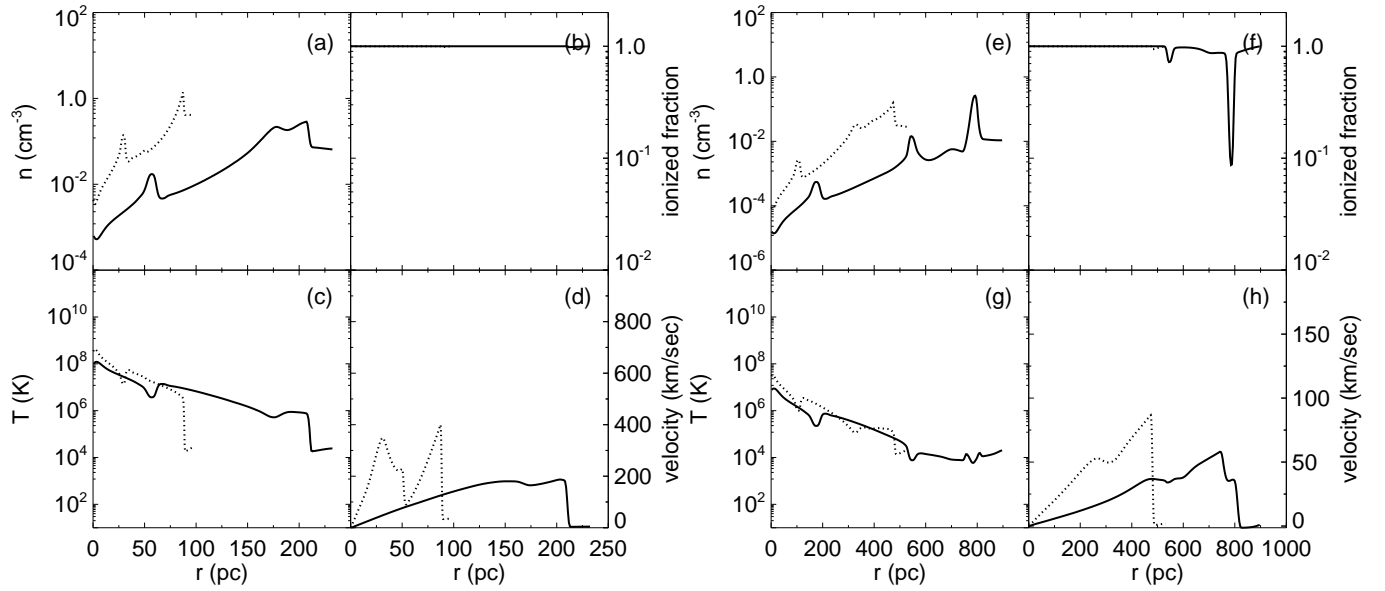


FIG. 5.— Later evolution of the  $260 M_{\odot}$  pair-instability supernova in halo 1. Panels (a) - (d): interaction of the  $260 M_{\odot}$  pair-instability remnant with the relic ionized core shock. Dotted:  $t = 19.8$  kyr; solid:  $t = 420$  kyr, respectively. Panels (e) - (h): flow profiles at 2.0 Myr (dotted) and 7.93 Myr (solid).

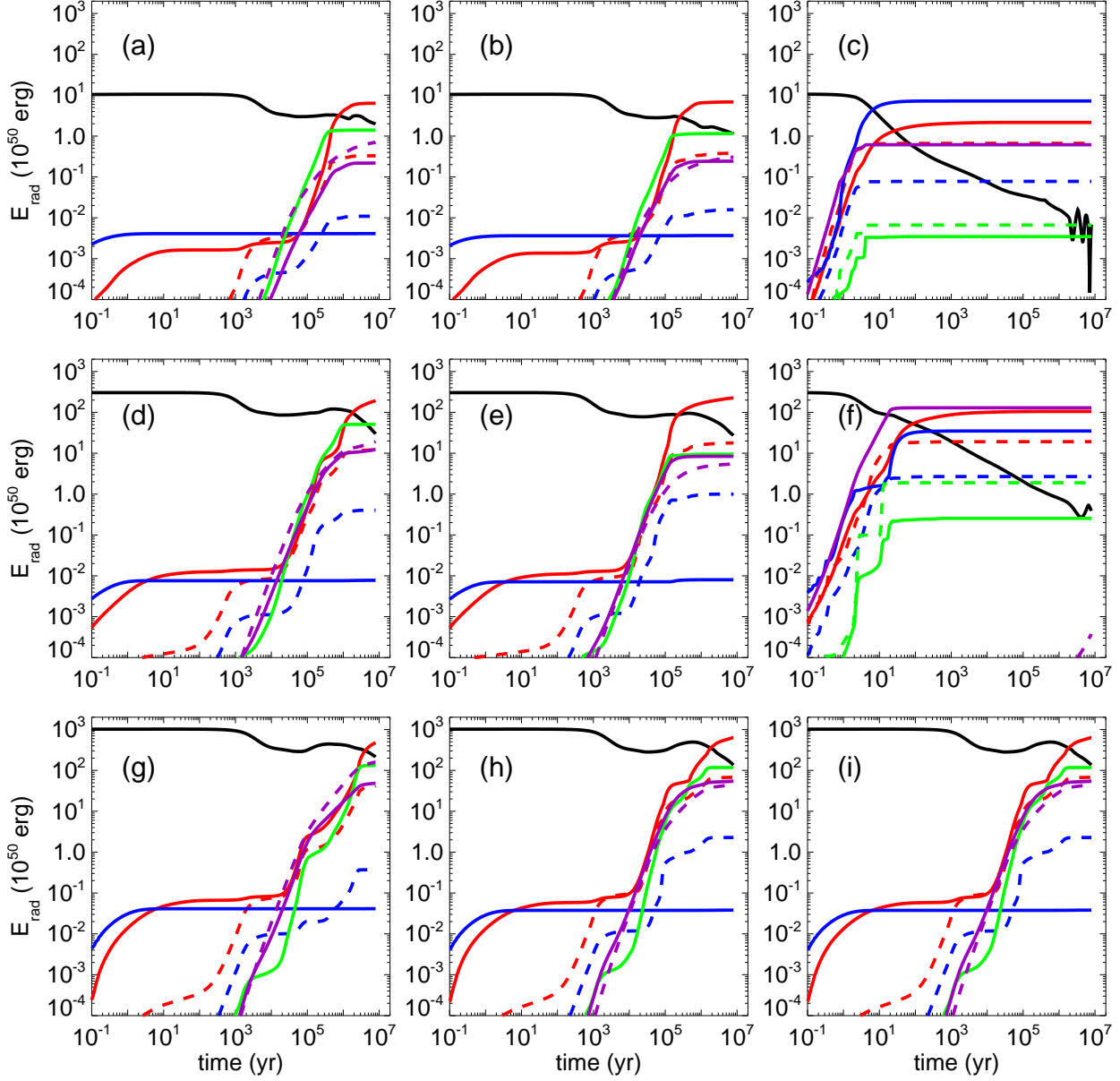


FIG. 6.— Radiative energy losses in all nine remnants *vs* time. Black solid: total kinetic energy; red solid: collisional excitation of H; red dashed: collisional ionization of H; blue solid: collisional excitation of He; blue dashed: collisional ionization of He; green solid: collisional excitation of  $\text{He}^+$ ; green dashed: collisional ionization of  $\text{He}^+$ ; purple solid: bremsstrahlung; purple dashed: inverse Compton scattering. Panels (a) - (c): 15 solar mass Type II SN in halo 1, halo 2, and halo 3, respectively. Panels (d) - (f): 40 solar mass hypernova in halo 1, halo 2, and halo 3, respectively. Panels (g) - (h): 260 solar mass pair-instability SN in halo 1, halo 2, and halo 3, respectively.

permit the flow to fully settle into an adiabatic Sedov-Taylor solution. By the time the remnant collides with the shell it has lost 70% of its kinetic energy.

#### 4.1.3. 19.8 kyr < t < 420 kyr: Collision with the Shell and the Radiative Phase

The 400 km s<sup>-1</sup> shock overtakes the 25 km s<sup>-1</sup> H II region shell at r = 85 pc at 59.5 kyr. Its impact is so strong that a second reverse shock forms and separates from the forward shock at 420 kyr. Both shocks are visible in the density and velocity profiles of Figure 5a at 175 and 210 pc. In reality, the interaction of the SN and shell is more gradual: the remnant encounters the tail of the shell at 60 pc at 19.8 kyr, at which time the greatest radiative losses begin, tapering off by 7 Myr with the formation of another reverse shock. Hydrogen Ly- $\alpha$  radiation dominates, followed by inverse Compton scattering, collisional excitation of He<sup>+</sup> and bremsstrahlung, but the remnant also collisionally ionizes H and He in the dense shell as evidenced by the sharp rise in ionization losses at 40 kyr. The rise in total kinetic energy at late times is due to the appearance of the dense shell of the H II region on the grid at 60 kyr, which cannot be separated from the remnant.

#### 4.1.4. t > 2 Myr: Dispersal of the Halo

Hydrodynamical profiles of the remnant at 2 Myr and at 7.93 Myr, the time to which the simulation was run, appear in Figures 5e-h. Figure 6g reveals that H Ly- $\alpha$  radiation drains the kinetic energy of the remnant out to 7 Myr and that collisional ionization continues to 4 Myr, well after the remnant has struck the shell. These additional losses occur as the supernova overtakes a series of smaller subsidiary shocks in the relic H II region visible just beyond the dense shell in the velocity profile of the left panel of Figure 2. One feature of these secondary collisions is the formation of a dense shell at 500 pc at 2 Myr that persists to 800 pc. The large recombination rates in this shell drop its ionization fraction to 0.08. Since densities elsewhere in the remnant are nearly 100 times smaller, this shell is likely the site of the H Ly- $\alpha$  losses for t > 2 Myr, which grow to 50% of the original energy of the blast.

The density plot at 7.93 Myr clearly shows that nearly all the baryons are ejected from the halo at velocities well in excess of the 2 - 3 km s<sup>-1</sup> escape speed. The blast scours gas from inside the virial radius, to densities much lower than in the H II region: 10<sup>-4</sup> cm<sup>-3</sup> as opposed to 0.1 cm<sup>-3</sup>. Only 10% of the energy of the blast survives radiative, gravitational, and adiabatic losses, but the momentum associated with this energy, together with strong relic ionized flows, still easily unbinds the gas from the halo. In these circumstances the dispersal of heavy elements into the surrounding intergalactic medium (IGM) is arrested when the remnant comes to pressure equilibrium with the relic ionized gas, typically at half the radius of the progenitor H II region (one or two kpc) (Greif et al. 2007).

Both Compton and free-free losses from the remnant decline after 3 × 10<sup>7</sup> yr, in general agreement with their respective cooling timescales at these densities, temperatures, and redshift (Kitayama & Yoshida 2005)

$$t_{\text{ff}} \sim 10^7 \left( \frac{n_{\text{H}}}{\text{cm}^{-3}} \right) \left( \frac{T_e}{10^7 \text{K}} \right) \text{yr}, \quad (21)$$

and

$$t_{\text{IC}} \sim 7 \times 10^6 \left( \frac{1+z}{20} \right)^{-4} \text{yr}. \quad (22)$$

At 2 Myr,  $n_{\text{H}} \sim 0.1 \text{ cm}^{-3}$ ,  $T_e \sim 10^5 \text{ K}$ , and  $z \sim 20$ , so  $t_{\text{ff}}$  and  $t_{\text{IC}} \sim 10^7 \text{ yr}$ .

The other six supernovae that explode in H II regions follow nearly identical evolutionary paths. Most of the initial blast energy goes into adiabatic expansion and then radiation upon impact with the ionized core shock in the fossil H II region from 10<sup>4</sup> - 10<sup>5</sup> yr. This timescale is set by the dynamics of the H II region: the core shock radii fall within a fairly narrow band set by the sound speed of the ionized gas, which is a weak function of temperature and varies little for the three types of progenitor. Radiative losses at these later times originate from both the remnant and the dense shell of the H II region. In all seven cases the SN destroys the halo: baryon densities interior to the virial radius fall below 10<sup>-4</sup> cm<sup>-3</sup>.

## 4.2. Blasts in Neutral Halos

We show in Figures 7 and 8 four stages of evolution for a 40 M<sub>⊙</sub> hypernova in halo 3, the most massive halo. The H II region is trapped so close to the star that the halo is essentially neutral and undisturbed when the star explodes.

### 4.2.1. t < 1 yr: Free-Expansion Driven Shock

As before, the leading edge of the expansion promptly heats to extremely high temperatures, this time to approximately 10<sup>10</sup> K. This is somewhat less than in the PISN because of the inertia of the surrounding medium. Although the edge of the shock is again completely ionized, it fails to jet forward as before because the ambient densities are so large, 10<sup>7</sup> cm<sup>-3</sup> instead of 0.1 cm<sup>-3</sup>. The shock strongly radiates, primarily by bremsstrahlung and excitation of He, although the latter falls off rapidly as shown in Figure 6f. Unlike PISN in the H II region, this blast loses large amounts of energy at very early times, 3 × 10<sup>50</sup> erg by 1 yr. At 0.301 yr the density profile is still mostly that of a homologous free expansion, but by 3.01 yr it has leveled out and a reverse shock can be seen in the velocity at 0.03 pc. At this radius the blast has swept up several times its own mass in the neutral halo. The abrupt rise in collisional excitation and ionization losses in He<sup>+</sup> at t ~ 1 yr coincides with the breakthrough of the dense shell, at 0.03 pc in Figure 7a, by the reverse shock, which requires 10<sup>50</sup> erg.

### 4.2.2. t < 20 yr: Early Radiative Phase

The second jump in He<sup>+</sup> excitation and ionization cooling at 20 yr in Figure 6f occurs when the reverse shock sweeps through and completely ionizes the dense interior of the fireball. From t = 2 - 20 yr, both adiabatic expansion and radiation drain two thirds of the energy from the blast in roughly equal proportions. The remnant exhibits the first of several Chevalier phases at 7.45 yr: a forward and reverse shock separated by a contact discontinuity is visible in Figure 7e. Bremsstrahlung losses level out after 20 yr because over the previous 10 yr the density of the shocked gas falls by a factor of 5 and cools below 10<sup>8</sup> K. This is again consistent with the free-free cooling time predicted by eq 21 for  $n_{\text{H}} \sim 2 \times 10^6 \text{ cm}^{-3}$  and  $T_e \sim 3 \times 10^9 \text{ K}$  at 0.3 yr.

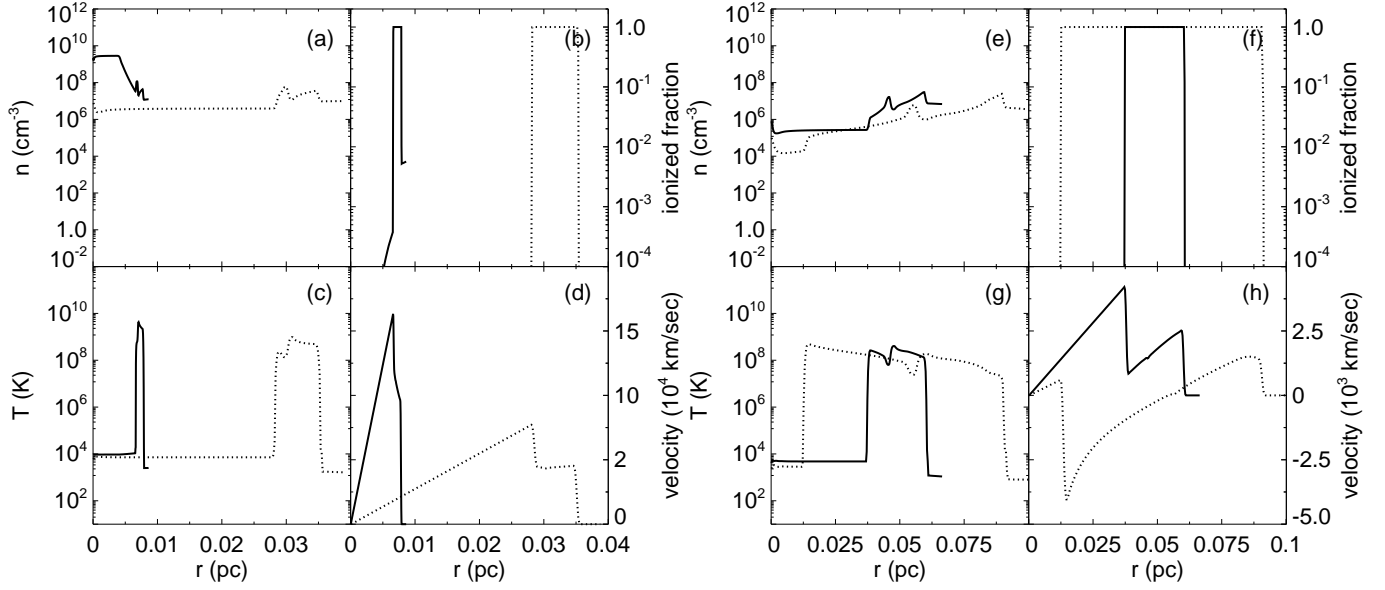


FIG. 7.— Early evolution of the  $40 M_{\odot}$  hypernova in halo 3. Panels (a) - (d): early free expansion. Solid: 0.301 yr; dashed: 3.01 yr. Panels (e) - (h): formation of the first reverse shock. Solid: 7.45 yr; dashed: 17.4 yr.

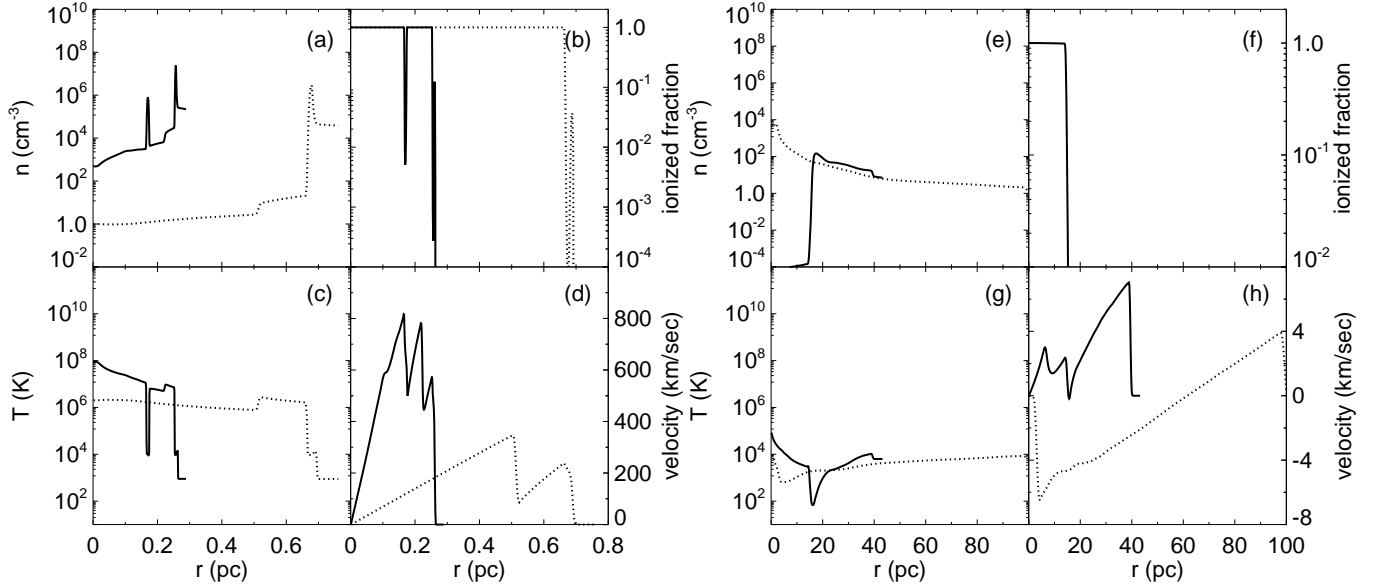


FIG. 8.— Later evolution of the  $40 M_{\odot}$  hypernova in halo 3. Panels (a) - (d): multiple strongly radiatively-cooling shocks. Solid: 214 yr; dotted: 1348 yr. Panels (e) - (f): fallback of the remnant to the center of the halo. Solid: 2.14 Myr; dotted: 6.82 Myr.

#### 4.2.3. $100 < t < 5000$ yr: Late Radiative Phase

The inertia of the neutral halo rapidly slows the blast, allowing time for a series of reflecting shocks to reverberate between the edge of the blast and the center of the interior. Reverse shocks continue to break off from the leading shock as it plows up more of the neutral halo and is overtaken by reflected shocks emerging from the interior. Flow profiles of this process are shown in Figures 8a-d. At 214 yr a new reverse shock in the density profile

at 0.25 pc is about to break away from the forward shock as a reflected shock approaches it from behind. At 1350 yr these two structures merge into a new single Chevalier phase with another reverse shock about to depart toward the origin.

These crossing shocks form dense shells that rapidly recombine and become mostly neutral. The shells are luminous sources of H Ly- $\alpha$  emission, which cools them to 10000 K amidst the otherwise fully ionized and very

hot gas. They are the sites of the H Ly  $\alpha$  losses from the remnant from 50 to 5000 yr in Figure 6f that eventually amount to a third of the energy of the blast. In this period the kinetic energy of the remnant falls to 0.5% of the energy of the SN but at 5000 yr and 1.5 pc it still has sufficient momentum to expand.

#### 4.2.4. *Fallback*

We show in Figures 8e-h the remnant at 2 Myr and 7.93 Myr. At 2 Myr the remnant has devolved into a slow dense shell of warm neutral gas extending from 15 to 40 pc and surrounding a hot, ionized diffuse ( $\lesssim 10^{-4}$  cm $^{-3}$ ) interior. The inner surface of the shell soon falls back into the dark matter potential as shown at 7.93 Myr in 8e. The outer region of the shell ripples outward but at velocities well below that required for escape from the halo. By now the gas is fully neutral.

In contrast to blast models that 'fizzle' when initialized by thermal energy in massive neutral halos (Kitayama & Yoshida 2005), the free expansion in our model delivers enough impulse to the halo to seriously disrupt it out to 40 pc, even though the remnant retains less than 1% of the energy of the blast by 2 Myr. Although the baryons remain bound to the halo, the ejecta heavily enriches them with metals prior to fallback, radically altering their cooling and fragmentation timescales. We find that the baryons can rebound from the center more than once after their initial recollapse into the halo, with large, episodic infall rates onto the central black hole. This may constitute a mechanism for the rapid growth of supermassive black hole seeds at high redshift. The explosion and its metals remain completely confined to the halo, unable to enrich the early IGM.

As another example of fallback in a trapped explosion, the evolution of the 15  $M_{\odot}$  supernova in halo 3 is qualitatively similar to that of the hypernovae, but with a few differences. First, the free expansion slows more quickly because it has less energy. The reverse shock at first fails to fully detach from the forward shock and instead forms a dense shell that emits extremely intense He lines. By approximately 1.1 yr this radiation slows the forward shock, cooling it suddenly from  $1 \times 10^8$  to  $10^4$  K in just 3.5 yr, extinguishing bremsstrahlung x-rays at 6 yr and terminating all other radiative losses by  $t \sim 20$  yr. Afterwards, the blast loses kinetic energy only to adiabatic expansion and gravity. The remnant passes through a single Chevalier phase at  $t \sim 6000$  yr, after which the reverse shock propagates back to the center of the halo. The reverse shock is too weak to ionize the interior, and the reverberations back to the forward shock are too faint to form shells. The SN therefore remains mostly neutral. Gravity arrests its expansion at 2.5 pc at  $1.35 \times 10^5$  yr, and it falls back to the center of the halo. Helium lines from the semi-detached reverse shock shell dominate the radiation from this remnant, emitting 75% of the energy of the blast.

We show central infall rates associated with the fallback of the 15 and 40  $M_{\odot}$  remnants in halo 3 from  $10^6$  yr to  $2 \times 10^7$  yr in Figure 9. Infall occurs later in the more massive remnant because its greater explosion energy carries it farther from the center of the halo. There are three fallback phases in the 15  $M_{\odot}$  remnant over this time interval ranging from  $10^{-3}$  -  $10^{-2}$   $M_{\odot}$  yr $^{-1}$  in magnitude and from 1 - 2 Myr in duration. The three

episodes are punctuated by rebound from the core of the halo, which is not shown in the figure. The first infall phase of the 40  $M_{\odot}$  remnant manifests rates of  $3.5 \times 10^{-2}$   $M_{\odot}$  yr $^{-1}$  and lasts 1.5 Myr. These are not the only occurrences of fallback; our numerical models indicate several more will occur in less than a merger time. In addition to fueling rapid growth of a black hole, these episodes will thoroughly mix metals from the ejecta in the central regions of high density in the halo because the leading shocks are subject to dynamical instabilities during both rebound and collapse. However, we point out that fallback of the remnant to the center of the halo is distinct from accretion onto the black hole, whose rates are governed by angular momentum and radiation transport away from the central object. Future radiation hydrodynamical simulations will determine the rates which the black hole grows in mass.

Intense bursts of x-rays from the central black hole will likely accompany these periods of heavy accretion, ionizing and heating gas within the halo and perhaps driving strong H $_2$  formation. It is generally held that the broad I-fronts of black holes and quasars exert positive feedback on structure formation because H $_2$  formation is promoted in their partially ionized outer layers (e. g. Ricotti et al. 2001). However, this picture is complicated by the fact that the accretion shock might radiate strongly in UV, including the LW bands, which would suppress H $_2$  formation. Furthermore, recent work on the structure of quasar ionization fronts indicates that they are preceded by a 'T-front', or temperature front (Qiu et al. 2008). This is a layer of  $10^4$  K minimally-ionized gas formed beyond the broadened I-front of black holes and quasars by the few most energetic photons. These photons cause secondary ionizations in the pre-front gas that heat it but cannot sustain a large ionization fraction. The pre-heated gas might pre-empt H $_2$  formation that would otherwise occur when the outer layers of the I-front reaches it. Detailed numerical simulations will be required to resolve the thermal and chemical evolution of the gas in the vicinity of the seed black holes at the centers of large halos at high redshifts.

The importance of including the dark matter gravitational potential in primordial SN models is particularly clear in trapped explosions. We performed experiments in which we set the halo in hydrostatic equilibrium and then evolved the blast without force updates by the dark matter potential. In these tests, the remnant simply continues expanding and there is no fallback. This provides a good check of the gravitational physics on the expanding grid and attests to the necessity of including dark matter in the calculation.

#### 4.3. *Halo Destruction Efficiency*

We summarize the results of our explosion models in the left panel of Figure 10. Halos less massive than  $2.1 \times 10^6$   $M_{\odot}$  are destroyed by Population III stars as small as 15  $M_{\odot}$  (we reiterate that destruction of the halo refers to expulsion of its gas, not its dark matter). On the other hand, PISN disperse much larger halos, even the first that could cool by atomic lines ( $\sim 1.0 \times 10^7$   $M_{\odot}$ ). This in part is because the star preionizes the halo. Indeed, even lower-mass primordial stars finally eject more than 90% of the baryons from halos  $\lesssim 10^7$   $M_{\odot}$  because their H II regions impart considerable momentum to the

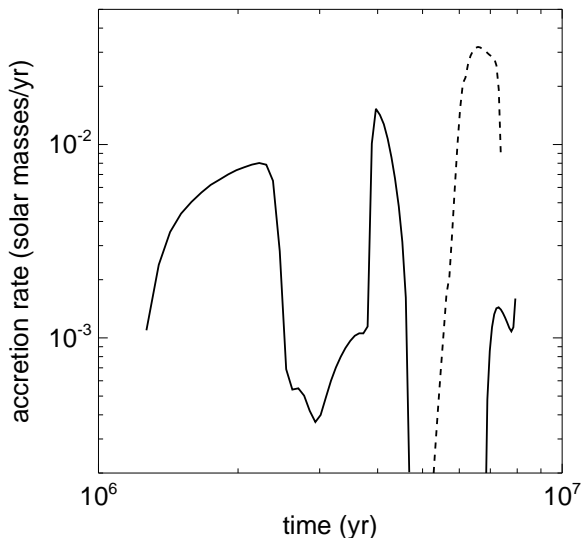


FIG. 9.— Infall rates  $4\pi\rho(r)v(r)r^2$  associated with fallback of the 15 and  $40 M_{\odot}$  remnants in halo 3. Solid:  $15 M_{\odot}$ ; dashed:  $40 M_{\odot}$

baryons prior to the explosion that facilitates breakout of the remnant into the IGM.

In failed H II regions, enough momentum from even modest explosions,  $10^{51}$  erg and  $3 \times 10^{52}$  erg, survives the enormous prompt radiative losses to disrupt halos out to a significant fraction of their virial radii. Nevertheless, we find that Type II supernovae and hypernovae are contained by halos more massive than  $1.0 \times 10^7 M_{\odot}$ , but will destroy less massive halos that cool mainly by molecular hydrogen. Recall that many primordial stars never explode: those lying between 50 and  $100 M_{\odot}$  and above  $260 M_{\odot}$  are not thought to exhibit any kind catastrophic mass loss (Heger & Woosley 2002). In these circumstances the halos are instead photoevaporated, with the loss of  $\sim 50\%$  of the gas rather than 95%, as expected for a SN. Although not all gas exits these halos, no subsequent star formation would follow for at least a merger time.

#### 4.4. Comparison to the Canonical Phases of Idealized Remnants

In the classic problem of a supernova blast in a uniform medium, idealized remnants evolve in four distinct phases: the free expansion, the Sedov-Taylor (ST) phase, the pressure driven snowplow (PDS), and the momentum conserving snowplow (MCS). Each stage can be loosely associated with a power law for the position of the shock as a function of time:  $R_S \propto t^{\eta}$ . In the early free expansion the flow is completely dominated by the momentum of each fluid element and this exponent is 1. Later, after the blast has swept up many times its own mass it consists of a self-similar adiabatic hot interior and non-radiative shock: the ST phase (Sedov 1959; Taylor 1950) in which  $\eta_{ST} = 2/5$ . As the remnant grows, the shock begins to be driven by the pressure of its hot, now nearly isobaric interior in addition to its own momentum because the postshock fluid velocity approaches that of the

shock (Cox 1972; Chevalier 1974). At about the same time, if the shocked gas can cool by radiation it collapses into a thin dense shell that accrues material as it ‘snowplows’ the interstellar medium (ISM). If the interior cannot radiatively cool in this pressure-driven snowplow (PDS) era its shock evolves according to  $\eta_{PDS} = 2/7$  (McKee & Ostriker 1977). Finally, if the interior loses energy both to  $PdV$  work and radiation, the remnant becomes a momentum conserving snowplow (MCS) whose analytical solution yields  $R_S \propto t^{1/4}$  (Oort 1951). The shell halts when it comes into pressure equilibrium with the ISM, after which it disperses and becomes indistinguishable from its surroundings.

We show in the right panel of Figure 10 shock position as a function of time for all nine remnants. All clearly exhibit an  $\eta \sim 1$  expansion at early times but depart from the canonical stages of ideal remnants in uniform media thereafter. This is not surprising for several reasons. When the reverse shock breaks away from the contact discontinuity at the end of the free expansion, it reverberates back and forth across the interior, heating it and never allowing it to relax to an ST phase, even though the leading shock does not radiate. This is likely why  $\eta < 2/5$  after the free expansion. When the remnant later mingles with the baryons that have been swept up into the H II region shock, it becomes strongly radiating without the formation of a thin shell. The curves taper somewhat more as the shock decelerates upon encountering the shell, as seen from  $10^4$  to  $10^5$  yr. The remnant cannot be disentangled from the strong fossil ionized flows thereafter.

On the other hand, supernovae in the dense cores of neutral halos depart from the standard behavior of ideal remnants in uniform densities because the cores are so stratified (with baryon densities falling by  $r^{-2.2}$ ), and because they radiate strongly from very early times. As a result, the free expansion ends in less than a year, and shocks reverberate through interior of the remnant even more frequently than in H II regions due to the inertia of the surrounding gas, again preventing the ST phase from materializing. Two stages of radiative loss without the formation of thin shells in the metal-free shocked gas then follow. Through all three stages adiabatic expansion also slows the remnant, with eventual fallback into the halo. Note that the plots in Figure 10 trace the position of the leading velocity front in the gas, which can continue outward into the halo even if the bulk of the remnant, which does not have a precise location, falls back toward the center. In short, we find that primordial supernovae do not conform to the usual paradigm for ideal remnants in uniform media.

Note from these profiles that the shock experiences brief periods of acceleration in neutral halos and may therefore be susceptible to Rayleigh-Taylor instabilities in three dimensions. Furthermore, the contact discontinuities separating forward and reverse shocks would also be prone to instabilities and breakup in multidimensional simulations (McKee & Ostriker 1977).

## 5. OBSERVATIONAL SIGNATURES OF PRIMORDIAL SUPERNOVAE

One trend that is immediately apparent in all nine remnants in Figure 6 is that adiabatic expansion losses precede radiative losses in blasts evolving in H II regions

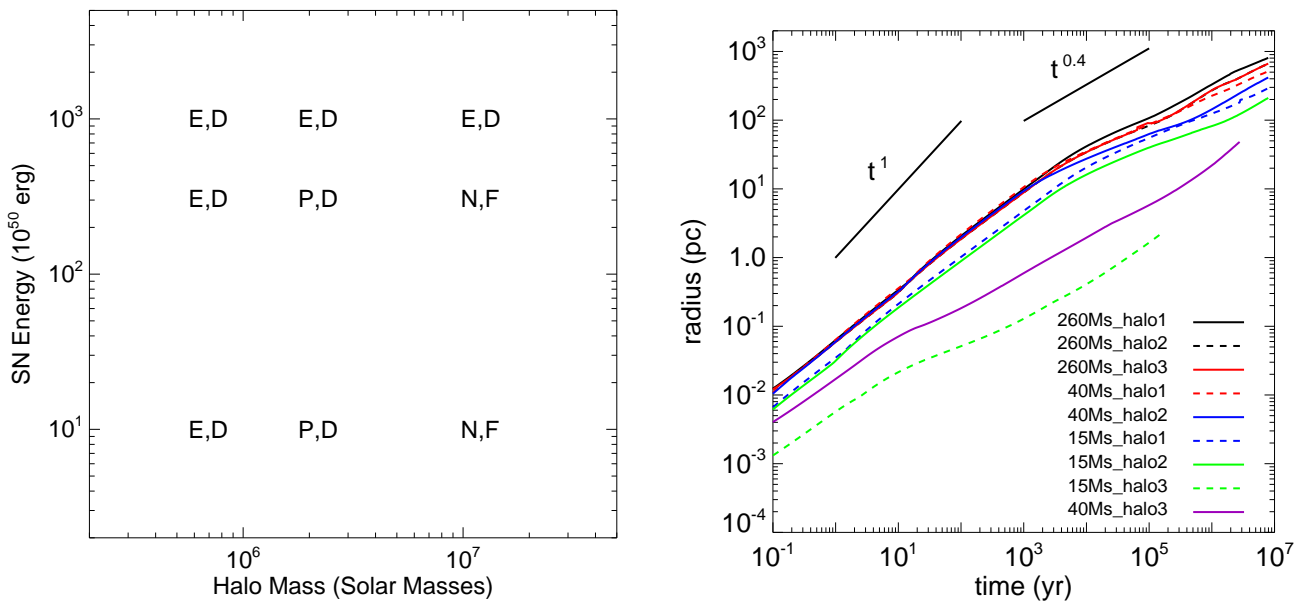


FIG. 10.— Left: eventual fate of a halo given the indicated explosion energy. The first letter refers to the final state of the halo prior to the explosion; E: photoevaporated; P: partly ionized, defined as the I-front not reaching the virial radius; N: neutral, or a failed H II region. The second letter indicates outcome of the explosion; D: destroyed, or F: fallback. Right: shock position *vs* time for the nine supernova remnants.

but are coincident in neutral halos. Another is that bremsstrahlung dominates energy losses in explosions in neutral halos but amounts to at most a few percent in H II regions. Inverse Compton scattering is greatest in the most powerful explosions in H II regions but virtually nonexistent in neutral halos, where the fireball cools before it can enclose large volumes of the CMB. In H II regions, H Ly- $\alpha$  finally dominates radiative losses from primordial remnants, with singly-ionized He excitation next in importance. Neutral He emission rivals or exceeds H Ly- $\alpha$  in less energetic blasts in neutral halos because He is not completely ionized. We plot luminosities due to excitation of H and He along with bremsstrahlung and IC for all nine remnants in Figure 11.

### 5.1. Luminosities in H II Regions

Type II supernovae and hypernovae in H II regions emit three flashes of Ly- $\alpha$  lines: the prompt flash when the free expansion forms a shock with its surroundings, a second flash as the reverse shock breaks free of the forward shock and ionizes the interior, and a final flash when the remnant collides with the dense H II region shell. Peak luminosities in the second and third flashes scale approximately with explosion yield:  $10^{38}$  erg s $^{-1}$  for the Type II supernova and  $10^{39}$  erg s $^{-1}$  for the hypernova and PISN. The third flash in more powerful explosions has twin peaks due to collisions with the smaller subsidiary shocks that lie just beyond the dense shell in the H II regions of more massive progenitors, as discussed in section 4.1.4. The contributions to each flash by H and He $^+$  are in proportion to their abundances. Because He is always singly ionized at later times it is absent in the second and third flashes. The second flash is consistently two orders of magnitude less intense than the third flash because the mass of the remnant is much lower than that of the dense shell and remnant combined.

It has been suggested that Ly- $\alpha$  photons from Population III stars are scattered by H in the early IGM, coupling its spin temperature to its kinetic temperature without heating the gas (Chen & Miralda-Escudé 2004). If the scattering region is not first heated by hard photons, the spin temperature would rapidly fall to the low kinetic temperature of the gas and the region would appear in absorption in 21 cm against the CMB. If more energetic photons later heat the scattering volume it would then appear in emission against the CMB, creating a brief absorption signal followed by a weak emission signal that is unique to Population III stars. Our findings indicate that the same may be true of the supernova remnant but in reverse: x-rays from the collision of the remnant and the dense shell die out before the Ly- $\alpha$  pulse, resulting in a strong 21 cm absorption signal preceded by weak emission against the CMB. Given that the lifetime of the main flash can exceed that of the star and that the scattering region can span several kpc proper, it may be possible to resolve them with the next generation of 21 cm observatories such as the *Square Kilometer Array* (SKA).

Although the Ly- $\alpha$  intensity of the first flash is at least a hundred times greater than in the next two, the actual energy released is minute due to its transience and is of little importance to the evolution of the free expansion. The large fluxes are in part numerical; they are emitted from the extremely large densities at the interface of the shock and the free expansion, which are not spatially resolved by the mesh. Artificial viscosity smears the enormous jump in density there over several zones, over which the temperature rises from a few thousand to several billion K. In one of the zones the temperature crosses the threshold for H and He line emission, activating these cooling channels for the entire zone when in reality they

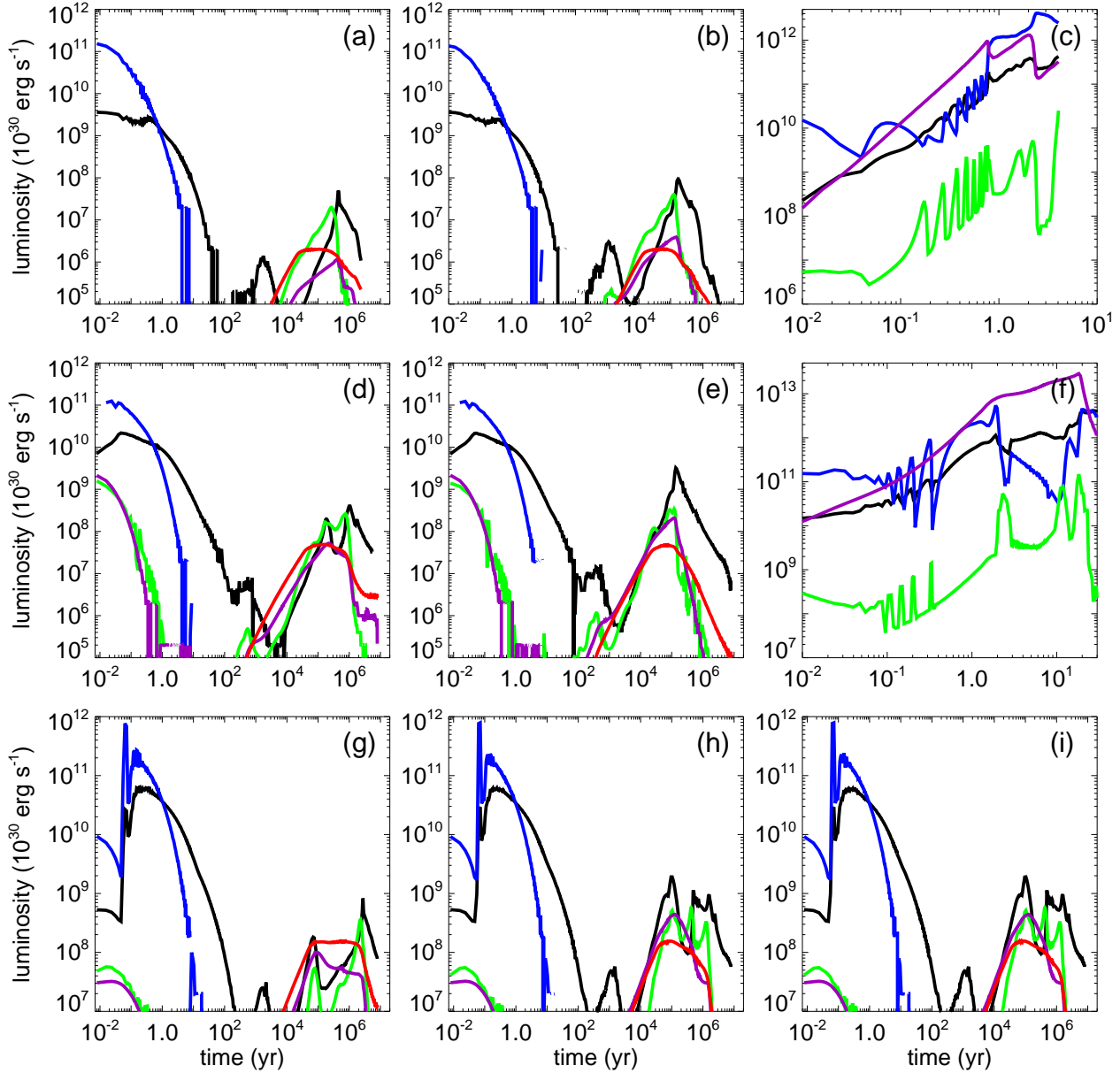


FIG. 11.— Luminosities of all nine primordial SN remnants *vs* time. Black: collisional excitation of H; blue: collisional excitation of He; green: collisional excitation of He<sup>+</sup>; purple: x-rays (bremsstrahlung); red: energy deposition rates into the CMB due to inverse Compton scattering. Panels (a) - (c): 15 solar mass Type II SN in halo 1, halo 2, and halo 3, respectively. Panels (d) - (f): 40 solar mass hypernova in halo 1, halo 2, and halo 3, respectively. Panels (g) - (i): 260 solar mass pair-instability SN in halo 1, halo 2, and halo 3, respectively. Note the different energy and time scales in panels (c) and (f), which describe the trapped explosions. As discussed in the text, the H and He line luminosities in the first pulse in H II region explosions should really be considered free-free losses.

originate from only an extremely thin shock layer that is a tiny fraction of the width of the zone. The Ly- $\alpha$  luminosity is thus overestimated by a factor roughly equal to the ratio of the widths of the zone and the shock; it is probably several orders of magnitude lower than free-free emission for  $t < 10$  yr. Little inaccuracy is introduced to the energetics of the ejecta by this artifact, not only because the energies involved are small. If excitational cooling of H and He are deactivated in this phase the shock simply remains hotter, with elevated free-free

emission rates that are nearly identical to the total rates when excitational cooling is included. Thus, nearly all the radiation in this era is really in x-rays, with peak luminosities of  $10^{41}$  erg s<sup>-1</sup>. Because the energy liberated is less than a millionth of the blast energy it does not appear in Figure 6. All three types of supernovae have similar luminosity profiles in H II regions in this era because the ejecta was assumed to have the same initial velocity profiles. Note that the energy of the first pulse, which is from the interaction of the shock and ambient

H II region, does not include the energy of radioactive decay in the ejecta, which is expected to be similar to that observed in SN today,  $\sim 10^{42}$  erg s $^{-1}$ .

Hypervolcanoes and PISN in H II regions emit a second x-ray flash during the collision with the dense shell. In contrast to the prompt flash, the second burst is longer,  $\sim 10^6$  yr with luminosities of  $10^{38}$  erg s $^{-1}$ . Type II supernovae emit only the second flash, with emission rates that are lower by two orders of magnitude. The durations of the second x-ray pulse and the inverse Comptonization of the CMB are again in agreement with the free-free and IC cooling times of eqs 21 and 22 for densities of 0.1 cm $^{-3}$  and temperatures of  $10^7$  K at 1 Myr. Although primordial supernovae were the first x-ray sources in the early universe they probably did not contribute to cosmological reionization (Tegmark et al. 1993). After examining early reionization by x-rays released by primeval supernovae, Kitayama & Yoshida (2005) concluded that unrealistically large explosion rates are required to create significant x-ray backgrounds at high redshift. However, prompt x-rays from blasts completely contained within neutral halos, although not visible to external observers, may drive strong H $_2$  formation that enhances the cooling and collapse of gas in the halos.

As noted earlier, Figures 6 and 11 show that cooling via inverse Compton scattering of cosmic microwave background photons contributes strongly to the loss of kinetic energy in supernova remnants evolving in H II regions. In some cases, such as the one shown in Figure 6g, it is more than 10% of the overall energy loss, but more generally only a few percent of the supernova's kinetic energy is deposited into the CMB. The strength of this cooling component is due to the high energy density of the CMB at the redshifts of these SN, and has been predicted by previous work (Tegmark et al. 1993; Voit 1996; Madau et al. 2001). One result will be a distortion of the CMB due to the Sunyaev-Zel'dovich effect, predicted to be on the order of  $\delta y \sim \text{few} \times 10^{-6}$  (Oh et al. 2003). The angular size of a given HII region and supernova remnant at  $z \sim 20$  is quite small, however – on the order of 100 kpc (comoving), which corresponds to an angular size of a few arc seconds. While individual Pop III supernovae would be essentially impossible to detect in the SZ with current telescopes, clusters of supernovae would create spectra distortions with a power spectrum that can be predicted by making assumptions about clustering bias. We have examined the assumptions made by Oh et al. (2003), and our results for radiative losses due to inverse Compton scattering are generally much lower than their predictions of 30-100% of the supernova kinetic energy, suggesting that their results would be an upper bound on the contribution of Population III supernovae to the SZ effect. Indeed, recent work by O'Shea & Norman (2007) suggests that the vast majority of Population III stars will form in halos with virial temperatures below  $10^4$  K, with a contribution to the angular power spectrum somewhere between cases B and C of Oh et al. (shown in Figure 1 of their paper). This implies that contributions to the SZ effect from Population III SN would be negligible in comparison to that from galaxy clusters, making them extremely difficult to detect.

## 5.2. Radiation from Neutral Halos

TABLE 6  
MASS OF ENRICHED BARYONS

halo	Type II SN	Hypervolcano	PISN
1	8.59E+5 $M_\odot$	1.75E+6 $M_\odot$	5.35E+6 $M_\odot$
2	4.35E+5 $M_\odot$	1.61E+6 $M_\odot$	3.38E+6 $M_\odot$
3	8.84E+4 $M_\odot$	1.61E+5 $M_\odot$	3.38E+6 $M_\odot$

Luminosity profiles for blasts in neutral halos exhibit a single peak lasting from 2 - 20 yr that is dominated by free-free and He line emission. The duration and peak intensity both scale with explosion energy: 2 yr and  $4 \times 10^{42}$  erg s $^{-1}$  for the Type II SN and 20 yr and  $2 \times 10^{43}$  erg s $^{-1}$  for the hypervolcano. Approximately 75% percent of the blast energy is lost in this one burst of radiation, which emanates from a volume less than 0.1 pc in radius. Again, these luminosities originate from the shock and not the radioactive decay of the ejecta. The luminosity of the shock in the Type II SN is comparable to that due to decay in sn today.

Line emission from the 15  $M_\odot$  and 40  $M_\odot$  SNR in halo 3 exhibits rapid oscillations in the first year on periods of a few days. This interesting phenomenon is due to the reverse shock that is attempting to break free of the contact discontinuity. Just as it does so, its densities and temperatures rise, with a sharp increase in line emission which then cools the shock. Losing pressure support, the reverse shock retreats toward the contact discontinuity in the frame of the flow until gas from the interior again builds at the interface and causes the shock to break free, beginning the cycle once more. Oscillations in standing radiative shocks are well understood in a variety of astrophysical contexts (Chevalier & Imamura 1982; Imamura et al. 1984; Anninos et al. 1997). The amplitudes of these variations in our luminosity profiles clearly demonstrate the reverse shock to be the origin of almost all the atomic lines for  $t < 1$  yr. Although not shown for brevity, oscillations are also present in the ionization cooling rates, again revealing the reverse shock to be their origin. Corresponding variations in the x-rays are absent because they originate from the shocked gas on the other side of the contact discontinuity.

Because the fireball cools fairly deep inside the halo, few of its x-rays are likely to escape into the IGM. In ambient densities of  $10^7$  cm $^{-3}$ , the mean free paths of 100 eV and 1 keV photons are  $1.7 \times 10^{-7}$  and  $3 \times 10^{-4}$  pc, respectively, so they would downscatter in energy many times before exiting the halo. It is possible that the x-ray photons would promote the formation of molecular hydrogen in the suppressed remnant, but this would be transient and only operate at intermediate radii. The resultant cooling would be much less important than the metal-line cooling near the center of the halo. As shown in Figure 11, confined explosions deposit little energy into the CMB because they cool before enclosing an appreciable volume of background photons. The visibility of atomic lines from deep inside the halo is also open to debate since the densities in the explosion envelope would cause many resonant scatterings for each photon. The photons may downscatter to radio wavelengths, as observed in hypercompact H II regions deep within molecular cloud cores (Churchwell 2002; Rodríguez 2005). Detailed calculations of Ly- $\alpha$  radiative transfer are neces-

TABLE 7  
AVERAGE METALLICITY OF ENRICHED BARYONS

Halo	Type II SN	Hypernova	PISN
1	6.87E-3 $Z_{\odot}$	1.16E-2 $Z_{\odot}$	2.32E-2 $Z_{\odot}$
2	1.36E-2 $Z_{\odot}$	1.26E-2 $Z_{\odot}$	3.68E-2 $Z_{\odot}$
3	6.68E-2 $Z_{\odot}$	1.26E-3 $Z_{\odot}$	3.68E-2 $Z_{\odot}$

sary to evaluate the 21 cm footprint of these explosions.

### 5.3. Optical/IR Light Curves

In our discussion we have neglected the optical/IR flash due to the radioactive decay of the ejecta, which would compete with the early radiation flash from the shock in both H II regions and neutral halos. Since nucleosynthetic yields are not well determined for these primordial events, we compare the peak optical luminosities of supernovae in the local universe to the first x-ray peaks in our simulations. First, it is worthwhile to note that at early times the ejecta is optically thick to its own decay photons, which diffuse out through the envelope. If we adopt the simple argument that the optical/IR flash reaches its peak when the radiation diffusion timescale through the envelope is equal to the age of the remnant, we find that (Arnett 1982; Pinto & Eastman 2001)

$$t_{\text{peak}} = \left( \frac{\kappa M_{\text{ej}}}{7cv_{\text{ej}}} \right)^{\frac{1}{2}}, \quad (23)$$

where  $M_{\text{ej}}$  and  $v_{\text{ej}}$  are the ejecta mass and peak velocity, respectively. Commonly used values of the opacity  $\kappa$  range from 0.1 - 0.4, depending on the inclusion of heavier element lines in addition to Thomson scattering. Assuming ejecta masses of 13 - 50  $M_{\odot}$  and shock speeds of 25000 km s<sup>-1</sup>, the light curves peak as early as 25 days and as late as 100 days, so they will compete with the early bremsstrahlung pulse.

Type Ia supernovae peak luminosities are clustered around  $9.6 \times 10^9 L_{\odot}$  (e. g. Branch & Tammann 1992) but those of Type II supernovae vary from 0.4 -  $4 \times 10^9 L_{\odot}$  (Tammann & Schroeder 1990). Maximum x-ray luminosities in our models fall between  $2.6 - 7.8 \times 10^7 L_{\odot}$ , hundreds of times lower than the optical/IR curves. However, the x-ray pulse lasts for 2 - 4 yr, approximately ten times longer than the decay flash. We conclude that visible and IR radiation outshine the x-rays but that the x-rays outlive the optical glow. As discussed in the previous subsection, atomic cascades in neutral halos likely downscatter these photons to much lower energies.

## 6. CHEMICAL ENRICHMENT

We find the early emergence of a Chevalier phase in all our models to be a predictor of efficient metal mixing at small radii in both H II regions and in neutral halos. In three dimensions, the susceptibility of the contact discontinuity separating the reverse and forward shocks to breakup (Cioffi et al. 1988) suggests that mixing would be prompt in neutral halos and be well underway by 25 pc in H II regions. However, the forward and reverse shocks may also exhibit Rayleigh-Taylor instabilities. This would enhance mixing in the outer remnant and perhaps allow ambient gas to reach the center as the reverse shock propagates through the interior. This

is in contrast to earlier work (Greif et al. 2007), whose numerical resolution could not address these phenomena.

How much gas is enriched by metals in these models, and to what levels? In H II regions that completely break out of the halo, the processes just described would enrich only half of the baryons originally interior to the virial radius of the halo, since the remainder are swept up into a dense shell 100 pc from the star. The degree to which the shell would be contaminated is yet to be determined, and is the focus of three-dimensional multiscale calculations now under development. Even more gas will be enriched as the shell and remnant expand together and then stall, typically at half the final radius of the H II region. In cases where the H II region exits the halo, we estimate the mass and metallicity of the enriched gas by assuming the SN ejecta is uniformly mixed with all the baryons interior to the stall radius. If the I-front ionizes only part of the halo, we approximate the final radius of the remnant from its deceleration beyond the virial radius and assume the ejecta to mix with all the gas inside this region. Finally, in neutral halos disrupted by the blast we consider the gas displaced by the remnant prior to fallback to be well mixed, which will be true after repeated episodes of infall and rebound in the dark matter potential. Estimates of the mass and metallicity of enriched gas in each model are tabulated in Tables 6 and 7.

Explosions in both H II regions and neutral halos enrich  $10^5$  to  $5 \times 10^6 M_{\odot}$  of gas with metallicities ranging from  $7 \times 10^{-3}$  to  $7 \times 10^{-2} Z_{\odot}$ . This is well above the critical metallicity believed to result in a rollover from high-mass to low-mass star formation in the early universe (Bromm et al. 2001; Mackey et al. 2003; Smith & Sigurdsson 2007). There are two modes of chemical enrichment in our models. Metals are either propagated far into the IGM, not returning to the halo in less than a merger time, which is  $\sim 20$  Myr at this epoch, or are confined deep within the parent halo. As Greif et al. (2007) point out, when metals escape into the IGM they preferentially migrate into voids of low density and do not influence star formation until they either recollapse into the halo or merge with a different one. However, the remnant itself could also be prone to breakup and clumping after colliding with the H II region shell, possibly triggering a second prompt generation of star formation in the enriched gas. These stars would reside in the outer regions of the halo, at radii of 100 - 200 pc. The implications of this novel mechanism for global star formation at high redshifts remain to be investigated with three-dimensional models that include metal line cooling. Type II and pair instability supernovae would imprint very different nucleosynthetic signatures on their descendants, which is important to surveys of ultra and extremely metal-poor stars in the galactic halo.

Immediate low-mass star formation is probable when metals are confined to the halo, given the short cooling and free-fall times in gas at densities of  $10^4 - 10^5 \text{ cm}^{-3}$  and metallicities of 0.01 solar. Approximately  $10^5 M_{\odot}$  of baryons are enriched to these levels, and it is conceivable that this gas could cool and fracture into a swarm of less-massive and long-lived stars that are confined to radii of 10 - 20 pc by the dark matter potential of the halo. Star formation would be complicated by the presence

of a central black hole with large x-ray luminosities fueled by fallback into the halo. Nonetheless, this scenario raises the intriguing possibility of globular cluster formation at high redshifts, various mechanisms for which have been studied in the past 40 years (Peebles & Dicke 1968; Peebles 1984; Kravtsov & Gnedin 2005).

## 7. DISCUSSION AND CONCLUSIONS

Primordial supernovae can be more damaging to cosmological minihalos than previous studies suggest when they are properly initialized with kinetic rather than thermal energy. This is primarily because the momentum of the ejecta cannot be radiated away, even when radiative cooling is highly efficient, as in partially ionized or neutral clouds. Even blasts that are trapped by massive halos severely disrupt them, mixing their interiors with metals and creating massive fallback onto any black hole that remains. Population III stars of lower mass that are capable of explosions ( $15 - 40 M_{\odot}$ ) easily destroy halos  $\lesssim 10^7 M_{\odot}$  but not more massive ones, in part because they cannot preionize them. On the other hand, primordial stars from  $140 - 260 M_{\odot}$  will destroy halos even more massive than  $10^7 M_{\odot}$  in pair instability supernova blasts. To a good approximation, any supernova will destroy any halo less massive than  $10^7 M_{\odot}$  when photoevaporation of the halo prior to the blast is taken into account.

Primordial supernovae evolve in one of two ways. Blasts in H II regions remain free expansions out to several pc and are decelerated first by adiabatic losses and then later by radiative losses. In addition to the light curve of the radioactive decay of their ejecta, these remnants radiate strongly upon collision with the dense shell of the H II region, usually by  $10^4 - 10^5$  yr. While most of their luminosity is in atomic H and He lines, particularly powerful blasts in H II regions can channel up to 20% of their energy into the CMB. Explosions in ionized halos evacuate gas from their virial radii to densities below  $10^{-4} \text{ cm}^{-3}$ . Our models are in qualitative agreement with earlier one-dimensional Lagrangian and three-dimensional smoothed particle hydrodynamics (SPH) calculations of Type II and pair instability SN in primordial H II regions. Our results are also consistent with early one-dimensional calculations of supernova blasts in uniform diffuse media (Chevalier 1974; Cioffi et al. 1988): they too manifest reverse shocks that separate from forward shocks at relatively small radii and exhibit multiple shock reflections throughout the interior.

On the other hand, blasts in nearly neutral halos promptly radiate most of their kinetic energy as x-rays but retain sufficient momentum for the ejecta to reach radii of  $10 - 20$  pc. These contained explosions leave little observational footprint but radically alter the evolution of gas within the halo, first by contamination with heavy elements and then by successive cycles of fallback and rebound. This is a departure from earlier supernovae models in neutral halos initialized with thermal rather than kinetic energy that is radiated away before launching any flow out into the halo. Again, in agreement with earlier work by Chevalier (1974) and Cioffi et al. (1988), we find that neither explosion pathway is well represented by the canonical phases of idealized remnants in uniform media (Sedov-Taylor, PDS, or MCS). In all cases inclusion of the dark matter potential is crucial; models would

otherwise fail to capture fallback in trapped explosions or erroneously predict expansion of the remnant until it achieves pressure equilibrium with the IGM.

Primordial supernovae occurred in neutral halos only if the halo was  $\gtrsim 10^7 M_{\odot}$  and the progenitor was not very massive. Given that stars normally form by  $\text{H}_2$  cooling well before the halo reaches this mass, is it likely that such blasts ever happened? The answer is yes if one considers halos at slightly later redshifts in rising Lyman-Werner backgrounds, whose effect is to postpone star formation in halos until they reach larger masses and become self-shielded to photodissociating photons (Machacek et al. 2001; O'Shea & Norman 2007; Wise & Abel 2007c). Numerical surveys indicate that when stars form in more massive halos whose virial temperatures approach the threshold for atomic line cooling, they still do so by molecular hydrogen cooling and are subject to the range in masses examined in this paper (O'Shea & Norman 2007). It is probable that explosions and fallback in more massive halos were more common at somewhat lower redshifts ( $15 - 20$ ) than those of the very first stars. We also point out that there are a greater range of spin parameters for star-forming halos than are sampled in current studies. Halos with higher angular momenta exhibit markedly lower central infall rates (O'Shea et al. 2005) that lead to much less massive stars. Finally, since the processes that halt accretion onto primordial stars remains poorly understood, low-mass supernovae in relatively massive halos cannot be ruled out.

The recent discovery of the first potential pair instability supernova ever observed (Smith et al. 2007) lends hope that this sort of explosion may have occurred in the high redshift universe. Population III PISN might be seen at moderate redshift ( $z \sim 6$ ) with current technology (Scannapieco et al. 2005), or out to significantly higher redshift with the *James Webb Space Telescope* (Weinmann & Lilly 2005). Scannapieco et al. use the KEPLER code to create mock supernova light curves and demonstrate that the typical luminosities of pair instability supernovae are not much brighter than standard Type Ia supernovae. However, they remain brighter for much longer periods of time and have distinctive spectral features, making them easy to discriminate from standard Type Ia or Type II supernovae. Unfortunately, time dilation may make the light curves of extremely high redshift supernovae difficult to detect, especially those powered by the pair instability, since they have long evolutionary times in the rest frame. Their observation would require very different survey strategies than those employed in low redshift supernova searches. Furthermore, the predicted Population III supernova rate varies widely depending on a range of basic assumptions (Weinmann & Lilly 2005; Wise & Abel 2005; Mesinger et al. 2006).

If Population III supernovae are ever observed, they may be useful probes of their immediate environments. Peculiar features in a supernova light curve can be exploited to infer the properties of circumstellar gas (Smith & McCray 2007). If Population III stars are rapidly rotating, they may explode as gamma ray bursts (Bromm & Loeb 2006) and could be used to probe the interstellar medium of the halos in which they form, as has been done in the  $z < 4$  universe (Chen et al. 2005;

Prochaska et al. 2006, 2007).

The ionization front of the progenitor itself would also be prone to violent dynamical instabilities in three dimensions due to  $H_2$  cooling, forming gas clumps in the relic H II region with which the blast would interact (Whalen & Norman 2007a,b). They would be most prominent in H II regions trapped in massive halos, partly because D-type fronts better shield  $H_2$  from Lyman-Werner photons from the star and partly because R-type I-fronts that break free of halos would tend to photoevaporate any clumps that may have formed, although numerical simulations indicate that some would survive (Whalen & Norman 2007a,b). I-front instabilities may also drive turbulence in the surrounding medium. Both fragmentation and turbulence will enhance the mixing of metals in halos and should be included for self-consistency in future three dimensional models.

Molecular hydrogen and HD could also cause the remnant to cool and fragment, a process not addressed in these models. Explosions in ionized halos would sweep up  $H_2$  and HD that are rapidly forming in the relic H II region. However, molecular cooling would not occur until late times in our models because the remnant remains fully ionized and hot for several Myr, as shown in Figure 5f. At 7.93 Myr,  $H_2$  might form in the forward shock as it partially recombines and cools to 10000 K, forming a dense shell that might be prone to breakup. In all likelihood, prior instabilities, such as Rayleigh-Taylor instabilities in the shock, would pre-empt those due to  $H_2$  cooling, but the radiative losses might still be relevant to the kinematics of the remnant. Molecular hydrogen cooling might also be viable in trapped explosions. Figures 8b and f show that the leading shock in the contained blast recombines and cools at much earlier times, at about the same time instabilities would erupt in the contact discontinuity. Rayleigh-Taylor instabilities in the reverse shock and Vishniac instabilities in the forward shock mediated by  $H_2$  cooling could evolve together, destroying the shell from within and without.

In the absence of magnetic fields in the vicinity of the progenitor, how would the free expansion interact with the H II region or neutral halo? Simple collisional cross section arguments imply that the ejecta particles would travel to great distances with little deflection by the surrounding gas unless magnetic fields mediate hydromagnetic interactions between the blast and its environment. If no primordial fields were present, the ejecta might interact differently with the halo than predicted by the fluid equations, which are predicated upon mean free paths in the flow being far shorter than characteristic lengths in the flow itself. Nevertheless, for now it is reasonable to suppose that magnetic fields arise due to the Weibel instability (e. g. Medvedev 2007), effectively coupling the two plasma streams. This mechanism has been invoked to explain the origin of GRB afterglows (Medvedev et al. 2007).

An important phenomenon not noted in earlier surveys of primordial supernovae are the large central infall rates that can result from fallback when remnants fail to escape massive halos, in excess of  $10^{-2} M_{\odot} \text{ yr}^{-1}$  and lasting 1 - 2 Myr in some instances. Such infall, although less coordinated, would certainly appear in three dimensional simulations and lead to rapid growth of the central

black hole. The growth would be episodic since bounce-back would periodically reverse the inflow, and three dimensional radiation hydrodynamical accretion simulations would be required to ascertain how much gas at the center of the halo would fall into the black hole. Nevertheless, this mechanism may provide the means whereby black holes of several thousand solar masses could form in pregalactic structures at  $z \sim 20$ , which numerical studies suggest could be the origin of the supermassive black holes occupying the centers of most massive galaxies today (Li et al. 2007). Periodic accretion onto the black hole would emit bursts of radiation from the halo that might over time contribute to an x-ray background at high redshifts and strongly affect the thermal and chemical properties of the halo.

One alternative to this scenario is that gas in the trapped explosion instead cools to tens of Kelvin by metal-line cooling and then fragments, forming many low mass stars whose peculiar motions are confined to the dark matter potential of the halo. Several tens of thousands of solar masses of gas could fuel low mass star formation in this manner. If large numbers of small stars can truly form in the halo the result could be a globular cluster 15 - 30 pc in diameter, the radii to which gas in the halo is disturbed by the blast. High dynamical range adaptive mesh refinement (AMR) simulations are necessary to determine if gas in the halo can fracture and collapse in this fashion.

Finally, our supernova models may hint at an alternative pathway for the assembly of the first primitive galaxies. Greif et al. (2007) find that the first supernovae preferentially expel metals into the voids interspersed among cosmological filaments. Since densities are relatively low there, the metals do not promote immediate star formation, and must generally await merger timescales to be taken up into a new generation of stars. If supernovae ejecta instead mix efficiently with the dense shells of relic H II regions and cause them to cool and fragment, a second generation of stars with different chemical abundance patterns might promptly form. Likewise, explosions trapped by massive halos could also create small populations of new stars before mergers with other halos. If so, the first primitive galaxies were assembled sooner, with more stars and different chemical abundances than in current cosmological models. Upcoming observations by the *James Webb Space Telescope* and *Thirty Meter Telescope* might discriminate between these two scenarios.

We thank the anonymous referee, whose detailed comments significantly improved the quality of this work. We also thank Ken Nomoto for providing us his supernova yields and Guillermo Garcia-Segura, Alex Heger, and Lars Bildsten for helpful discussions concerning these simulations. BWO was supported by a LANL Director's Postdoctoral Fellowship (DOE LDRD grant 20051325PRD4). This work was carried out under the auspices of the National Nuclear Security Administration of the U.S. Department of Energy at Los Alamos National Laboratory under Contract No. DE-AC52-06NA25396. The simulations were performed on the open cluster Coyote at Los Alamos National Laboratory.

## REFERENCES

- Abel, T., Bryan, G. L., & Norman, M. L. 2000, *ApJ*, 540, 39
- Abel, T., Bryan, G. L., & Norman, M. L. 2002, *Science*, 295, 93
- Abel, T., Wise, J. H., & Bryan, G. L. 2007, *ApJ*, 659, L87
- Abel, T., Anninos, P., Zhang, Y., & Norman, M. L. 1997, *New Astronomy*, 2, 181
- Alvarez, M. A., Bromm, V., & Shapiro, P. R. 2006, *ApJ*, 639, 621
- Anninos, P., Zhang, Y., Abel, T., & Norman, M. L. 1997, *New Astronomy*, 2, 209
- Arnett, W. D. 1982, *ApJ*, 253, 785
- Baraffe, I., Heger, A., & Woosley, S. E. 2001, *ApJ*, 550, 890
- Branch, D., & Tammann, G. A. 1992, *ARA&A*, 30, 359
- Bromm, V., Coppi, P. S., & Larson, R. B. 1999, *ApJ*, 527, L5
- Bromm, V., Ferrara, A., Coppi, P. S., & Larson, R. B. 2001, *MNRAS*, 328, 969
- Bromm, V., Yoshida, N., & Hernquist, L. 2003, *ApJ*, 596, L135
- Bromm, V., & Loeb, A. 2006, *ApJ*, 642, 382
- Chen, H.-W., Prochaska, J. X., Bloom, J. S., & Thompson, I. B. 2005, *ApJ*, 634, L25
- Chen, X., & Miralda-Escudé, J. 2004, *ApJ*, 602, 1
- Chevalier, R. A. 1974, *ApJ*, 188, 501
- Chevalier, R. A., & Imamura, J. N. 1982, *ApJ*, 261, 543
- Chugai, N. N., & Chevalier, R. A. 2006, *ApJ*, 641, 1051
- Churchwell, E. 2002, *ARA&A*, 40, 27
- Cioffi, D. F., McKee, C. F., & Bertschinger, E. 1988, *ApJ*, 334, 252
- Cox, D. P. 1972, *ApJ*, 178, 159
- Dwarkadas, V. V. 2005, *ApJ*, 630, 892
- Franco, J., Tenorio-Tagle, G., & Bodenheimer, P. 1990, *ApJ*, 349, 126
- Galli, D., & Palla, F. 1998, *A&A*, 335, 403
- Gao, L., Yoshida, N., Abel, T., Frenk, C. S., Jenkins, A., & Springel, V. 2007, *MNRAS*, 378, 449
- Greif, T. H., Johnson, J. L., Bromm, V., & Klessen, R. S. 2007, *ApJ*, 670, 1
- Hayes, J. C., Norman, M. L., Fiedler, R. A., Bordner, J. O., Li, P. S., Clark, S. E., ud-Doula, A., & Mac Low, M.-M. 2006, *ApJS*, 165, 188
- Heger, A. & Woosley, S. E. 2002, *ApJ*, 567, 532
- Imamura, J. N., Wolff, M. T., & Durisen, R. H. 1984, *ApJ*, 276, 667
- Johnson, J. L., Greif, T. H., & Bromm, V. 2007, *ApJ*, 665, 85
- Kitayama, T., & Yoshida, N. 2005, *ApJ*, 630, 675
- Kitayama, T., Yoshida, N., Susa, H., & Umemura, M. 2004, *ApJ*, 613, 631
- Kravtsov, A. V., & Gnedin, O. Y. 2005, *ApJ*, 623, 650
- Kudritzki, R. 2000, *The First Stars. Proceedings of the MPA/ESO Workshop held at Garching, Germany, 4-6 August 1999.* Achim Weiss, Tom G. Abel, Vanessa Hill (eds.). Springer, Li, Y., et al. 2007, *ApJ*, 665, 187
- Machacek, M. E., Bryan, G. L., & Abel, T. 2001, *ApJ*, 548, 509
- Mackey, J., Bromm, V., & Hernquist, L. 2003, *ApJ*, 586, 1
- Madau, P., Ferrara, A., & Rees, M. J. 2001, *ApJ*, 555, 92
- McKee, C. F., & Ostriker, J. P. 1977, *ApJ*, 218, 148
- Medvedev, M. V. 2007, *Ap&SS*, 307, 245
- Medvedev, M. V., Lazzati, D., Morsony, B. C., & Workman, J. C. 2007, *ApJ*, 666, 339
- Mesinger, A., Johnson, B. D., & Haiman, Z. 2006, *ApJ*, 637, 80
- Meynet, G., Ekstrom, S., Maeder, A., Hirschi, R., Chiappini, C., & Georgy, C. 2007, *ArXiv e-prints*, 709, arXiv:0709.2275
- Oh, S. P., Cooray, A., & Kamionkowski, M. 2003, *MNRAS*, 342, L20
- Oort, J. H. 1951, in *Problems of Cosmical Aerodynamics* (Dayton, Ohio: Central Air Document Office), p. 118.
- O'Shea, B. W., Abel, T., Whalen, D., & Norman, M. L. 2005, *ApJ*, 628, L5
- O'Shea, B. W., & Norman, M. L. 2007, *ApJ*, 673, 14
- O'Shea, B. W., & Norman, M. L. 2007, *ApJ*, 654, 66
- O'Shea, B. W., Bryan, G., Bordner, J., Norman, M. L., Abel, T., Harkness, R., & Kritsuk, A. 2004, *ArXiv Astrophysics e-prints*, arXiv:astro-ph/0403044
- Peebles, P. J. E. 1984, *ApJ*, 277, 470
- Peebles, P. J. E., & Dicke, R. H. 1968, *ApJ*, 154, 891
- Pinto, P. A., & Eastman, R. G. 2001, *New Astronomy*, 6, 307
- Prochaska, J. X., Chen, H.-W., & Bloom, J. S. 2006, *ApJ*, 648, 95
- Prochaska, J. X., Chen, H.-W., Dessauges-Zavadsky, M., & Bloom, J. S. 2007, *ApJ*, 666, 267
- Qiu, J.-M., Shu, C.-W., Liu, J.-R., & Fang, L.-Z. 2008, *New Astronomy*, 13, 1
- Ricotti, M., Gnedin, N. Y., & Shull, J. M. 2001, *ApJ*, 560, 580
- Rodríguez, L. F. 2005, *Massive Star Birth: A Crossroads of Astrophysics*, 227, 120
- Scannapieco, E., Madau, P., Woosley, S., Heger, A., & Ferrara, A. 2005, *ApJ*, 633, 1031
- Schaerer, D. 2002, *A&A*, 382, 28
- Sedov, L. I. 1959, *Similarity and Dimensional Methods in Mechanics*, New York: Academic Press, 1959,
- Smith, N., et al. 2007, *ApJ*, 666, 1116
- Smith, N., & McCray, R. 2007, *ApJ*, 671, L17
- Smith, B. D., & Sigurdsson, S. 2007, *ApJ*, 661, L5
- Stone, J. M., & Norman, M. L. 1992, *ApJS*, 80, 753
- Tammann, G. A., & Schroeder, A. 1990, *A&A*, 236, 149
- Taylor, G. I. 1950, *Proc. Roy. Soc. London A*, 201, 159
- Tegmark, M., Silk, J., & Evrard, A. 1993, *ApJ*, 417, 54
- Tominaga, N., Umeda, H., & Nomoto, K. 2007, *ApJ*, 660, 516
- Truelove, J. K., & McKee, C. F. 1999, *ApJS*, 120, 299
- Vink, J. S., de Koter, A., & Lamers, H. J. G. L. M. 2001, *A&A*, 369, 574
- Voit, G. M. 1996, *ApJ*, 465, 548
- Weinmann, S. M., & Lilly, S. J. 2005, *ApJ*, 624, 526
- Whalen, D., Abel, T., & Norman, M. L. 2004, *ApJ*, 610, 14
- Whalen, D., & Norman, M. L. 2006, *ApJS*, 162, 281
- Whalen, D. J., & Norman, M. L. 2007, *ArXiv Astrophysics e-prints*, arXiv:astro-ph/0703463
- Whalen, D., & Norman, M. L. 2007, *ArXiv e-prints*, 708, arXiv:0708.2444
- Wise, J. H., & Abel, T. 2005, *ApJ*, 629, 615
- Wise, J. H., & Abel, T. 2007, *ArXiv e-prints*, 710, arXiv:0710.3160
- Wise, J. H., & Abel, T. 2007, *ArXiv e-prints*, 710, arXiv:0710.4328
- Wise, J. H., & Abel, T. 2007, *ApJ*, 671, 1559
- Yoshida, N., Oh, S. P., Kitayama, T., & Hernquist, L. 2007, *ApJ*, 663, 687